



# Wavelet transformation induced multi-time scaling (WATMUS) model for coupled transient electro-magnetic and structural dynamics finite element analysis

Reza Yaghmaie<sup>1</sup>, Shu Guo<sup>1</sup>, Somnath Ghosh<sup>\*,2</sup>

*Department of Civil and Mechanical Engineering, Johns Hopkins University, 3400 N. Charles Street, Baltimore, MD 21218, United States*

Received 7 July 2015; received in revised form 9 January 2016; accepted 21 January 2016

Available online 4 February 2016

## Abstract

Multi-functional devices that integrate electromagnetic and mechanical fields are gaining importance in a wide variety of applications. The combined mechanical and electromagnetic regimes, encompassed in these structures, make it necessary to develop effective multi-physics analysis tools at a range of temporal scales. An important consideration is that the different fields governing multi-physics response may have large frequency discrepancies, e.g. the ultra-high electromagnetic frequencies and moderate vibration frequencies. Computational analyses of these discrepant frequency problems using conventional time integration schemes can become intractable. This paper develops a framework for coupling transient electromagnetic and dynamic fields to predict the evolution of electric and magnetic fields and their fluxes in a vibrating substrate undergoing finite deformation. It addresses the issue of time integration with large frequency ratios, by introducing a novel wavelet transformation induced multi-time scaling (WATMUS) method in the finite element framework. The method significantly enhances the computational efficiency in comparison with conventional single time scale integration methods. An adaptive enhancement of WATMUS scheme allows for the optimal wavelet bases in the transformation and integration step sizes. The accuracy and efficiency of the proposed WATMUS scheme is verified by comparing the results with the single time-scale simulations of the coupled transient electromagnetic nonlinear vibration problems.

© 2016 Elsevier B.V. All rights reserved.

*Keywords:* Wavelet; Multi-time scaling; Dynamics; Transient electromagnetics; Time integration; Adaptivity

## 1. Introduction

Multifunctional and intelligent structures are finding increasing use in a wide variety of commercial and defense applications [1,2]. Examples of applications include conformal load bearing antenna, deformable piezoelectric

\* Corresponding author. Tel.: +1 410 516 7833; fax: +1 410 516 7473.

E-mail address: [sghosh20@jhu.edu](mailto:sghosh20@jhu.edu) (S. Ghosh).

<sup>1</sup> Graduate Research Associate.

<sup>2</sup> M. G. Callas Professor.

sensors, flexible energy harvesting devices, stretchable electronics, MEMS, elastomer-based electromagnetic devices, to name a few [3,4]. Many of these devices implement coupled electro-magnetic (EM) and mechanical (ME) field problems in their design. The ME fields in many cases have significant effect on the EM signals. In some cases, the EM fields also cause forces e.g. the Lorentz force that affects the mechanical state. Load bearing antennae are subjected to mechanical vibrations, which have frequencies that are considerably different from those for the electro-magnetic field. For piezoelectric devices, coupling between the fields happens naturally since the piezoelectric material is able to convert mechanical energy to electrical energy and vice versa. Another application is electromagnetic metal forming processes [5,6] that represents contact-free high-speed forming, reaching strain rates  $\geq 10^3 \text{ s}^{-1}$ . These processes are driven by electromagnetic body forces due to the interaction of a magnetic field with the induced current. Analysis of multi-functional structures requires solution of multi-physics problems at a range of spatial and temporal scales. As the useful properties for materials are extended into combined mechanical and electromagnetic regimes, effective tools are necessary to analyze these complex systems.

Modeling coupled multi-physics problems, involving the evolution of EM fields in moving deformable media, while necessary is a significant challenge. In Section 5.1, an example has been solved to establish the need for coupled analysis when transient electro-magnetic problems are solved in a dynamically moving substrate. A limited number of coupled computational models are available in the literature. Numerical implementation of coupled electro-magneto-thermal systems of heterogeneous materials, involving the absorption of electromagnetic energy, its conversion to heat and changes in the electromagnetic material properties has been conducted in [7,8] using FDTD methods. Constitutive models, addressing magneto-mechanically coupled non-linear and hysteretic response of ferromagnetic shape memory alloys and dissipative ferroelectricity have been proposed in [9–13]. Return mapping algorithms in ferroelectricity have been developed in [14]. Finite element modeling of time dependent Maxwell's equations in dispersive media has been conducted in [15]. A general framework for electro-magneto-mechanical coupling in quasi-static problems has been conceived in [16,17]. Finite element analyses of electro-mechanically coupled problems for ferroelectric ceramics has been presented in [18,19]. A vector-valued electric potential formulation has been executed in [20] as an alternative to the scalar-valued potential approach for coupled electro-mechanical problems. A hybrid finite element scheme for non-linear electromechanical problems has been proposed in [21]. Adaptive goal-oriented *hp*-FE methods have been developed for electromagnetic problems with applications in dipole antenna in [22,23]. Coupled boundary and finite element simulations of nonlinear elastostatics problems have been conducted in [24] where the surrounding space is modeled using boundary elements. In a recent paper [25], the authors have developed a generalized framework for coupling transient electromagnetic and dynamic mechanical fields to predict the evolution of electric and magnetic fields and their fluxes in a vibrating substrate undergoing finite deformation. The framework is based on the theory of electromagnetics in deforming media [26–28].

A major challenge with solving many real applications of the coupled, transient electromagnetic, dynamic mechanical simulations is the high frequency ratio of electromagnetic to mechanical loadings, often greater than  $10^4$ . This requires, simulating a large number of electromagnetic cycles to reach a desirable state in the mechanical deformation. In conventional semi-discrete finite element simulations using single-scale time integration methods [29], each cycle is discretized into a number of temporal points to meet the stability requirements of integrating the higher frequency field. For high frequency ratios of EM–ME loading, this requirement poses significant challenges due to the largely discrepant temporal scales. Multi-time scaling methods, based on asymptotic expansions, have been discussed for Maxwell's equations in the absence of other fields in [30,31]. These methods may not provide any advantage over the single time scale computations due to the existence of two-way coupling between the temporal scales. Attempts to overcome this bottleneck through interpolation-based hierarchical modeling in [32] have not resulted in favorable results for history dependent problems. The almost-periodic temporal homogenization (APTH) operator [33,34], generally leads to very small time steps to preserve stability in the simulations and hence loses any efficiency advantage. Runge–Kutta exponential time discretization methods have good stability properties and have been applied to nonlinear wave equations in [35–39]. However they do not provide significant computational advantages in these problems.

There is a considerable need for effective multi time-scale resolved integration schemes, when modeling coupled multi-physics problem with disparate frequencies. This paper is aimed at addressing this need through the development of a wavelet transformation based multi-time scaling (WATMUS) method, thus overcoming the major deficiencies. The scheme was originally conceived for modeling fatigue problems in the context of crystal plasticity finite element simulations in [40–42]. The wavelet decomposition projects the high frequency response onto a low frequency

cycle-scale problem through wavelet basis functions for numerical integration. No assumption of scale separation is needed with this method. This paper is organized in the following sections. The framework for coupling transient electromagnetic and dynamic mechanical fields, based on developments in [25], is discussed in Section 2. A brief review of a few existing multi-time scaling methods is given in Section 3, followed by wavelet transformation induced multi-time scaling (WATMUS) method development in Section 4. Section 5 introduces the WATMUS method for coupled electro-magneto-mechanics with a brief review introduction of various multi-resolution wavelet families. Adaptive criteria to improve the accuracy and efficiency of the WATMUS algorithm are developed in Section 6, and numerical examples validating the WATMUS algorithm followed by examples on simulating ultra-high frequency transient electromagnetic fields in conductor structures undergoing cyclic dependent large mechanical vibrations are provided in Section 7. The paper ends with conclusions in Section 8.

## 2. FE model for coupled transient electromagnetic and structural dynamics problems

A comprehensive framework for solving the coupled transient electromagnetic and dynamic mechanical fields, based on the theory of electromagnetics in deforming media has been developed in [25]. The coupled model predicts the evolution of electric and magnetic fields in a substrate undergoing finite deformation under dynamic loading conditions. The mechanical loading influences the electromagnetic fields through changes in the geometric configuration of the conducting substrate. Mechanical field variables, in turn, can be affected by electromagnetically induced forces, e.g. the Lorentz force. For many applications, such as load-bearing antenna, the magnitude of the Lorentz force is negligible in comparison with the externally applied mechanical forces. Consequently, a one-way coupling between the two fields is considered, where only the EM variables are affected by the deformation of the structure. The Lagrangian formulation in [25], which maps Maxwell’s equations from spatial to reference material coordinates, is summarized next.

### 2.1. Governing equations in the reference configuration (Lagrangian description)

The deformation behavior of the conducting substrate undergoing finite deformation is modeled for a hyperelastic material under dynamic loading conditions. In Lagrangian mechanics, the reference configuration  $\Omega_0 (= \Omega(t_0))$  at a time  $t_0$  is expressed in terms of the material coordinates  $X_I$ ,  $I = 1, 2, 3$ , whereas the current configuration  $\Omega(t)$  at time  $t$  is represented by the current spatial coordinates  $x_i$ ,  $i = 1, 2, 3$ . The Cartesian components of the displacement vector in the material coordinates are expressed as:  $u_i(X_J, t) = x_i - \delta_{iJ}X_J$ . The deformation gradient tensor  $F_{iJ} = \frac{\partial x_i}{\partial X_J}$  characterizes the deformation of the material, and it is such that the Jacobian determinant  $J = \det(F_{iJ}) > 0$ .

The constitutive relation at finite strains for the hyper-elastic material is assumed to be neo-Hookean, for which the strain energy density function  $W$  can be expressed in terms of kinematic variables as:

$$W = \frac{1}{2}\lambda(\ln J)^2 - \mu \ln J + \frac{1}{2}\mu (C_{II} - 3) \tag{1}$$

where  $\lambda$  and  $\mu$  are Lamé constants, and  $C_{IJ} (= \frac{\partial x_k}{\partial X_I} \frac{\partial x_k}{\partial X_J})$  is the right Cauchy–Green deformation tensor. The stress–strain relation for finite strains is derived from the energy density expression in Eq. (1) where the components of second Piola–Kirchhoff tensor are obtained as:

$$S_{IJ} = J \frac{\partial X_J}{\partial x_m} \frac{\partial X_I}{\partial x_n} \sigma_{mn} = 2 \frac{\partial W}{\partial C_{IJ}} = \lambda \ln J C_{IJ}^{-1} + \mu(\delta_{IJ} - C_{IJ}^{-1}) \tag{2}$$

where  $\sigma_{ij}$  are components of the Cauchy stress tensors. The equilibrium equation for finite deformation theory in the reference configuration is expressed as:

$$\frac{\partial P_{iJ}}{\partial X_J} + \rho_0 b_i = \rho_0 \ddot{u}_i \tag{3}$$

where  $P_{iJ} (= \frac{\partial x_i}{\partial X_K} S_{KJ})$  are the components of the first Piola–Kirchhoff stress tensor,  $\rho_0$  is the density in the reference configuration and  $b_i$  is the body force per unit mass.

Maxwell’s equations, governing the evolution of EM variables for a conducting medium, are expressed in the current configuration (Eulerian description) as [26]:

$$d_{i,i} = q_e \quad \text{Gauss' law of electricity} \tag{4a}$$

$$b_{i,i} = 0 \quad \text{Gauss' law of magnetism} \tag{4b}$$

$$\varepsilon_{ijk} e_{k,j} = -\frac{\partial b_i}{\partial t} \quad \text{Faraday's law of magnetism} \tag{4c}$$

$$\varepsilon_{ijk} h_{k,j} = \frac{\partial d_i}{\partial t} + j_i^f \quad \text{Ampere's law} \tag{4d}$$

where  $d_i, b_i, e_i$  and  $h_i$  represent the Cartesian components of the electric displacement field vector, magnetic induction field vector, electric field and magnetic field strength respectively and  $q_e$  is the free charge density. The free charge current  $j_i^f$  is defined as:

$$j_i^f \triangleq j_i^c + q_e \dot{x}_i \tag{5}$$

where  $j_i^c$  is conducting current and  $\varepsilon_{ijk}$  is the Levi-Civita permutation symbol. The constitutive laws for an isotropic material without magnetization and polarization effects in the current configuration are given as:

$$d_i = \varepsilon e_i, \quad h_i = \frac{1}{\mu} b_i, \quad j_i^c = \sigma (e_i + \varepsilon_{ijk} \dot{x}_j b_k) \tag{6}$$

where  $\varepsilon, \mu$  and  $\sigma$  are material constants representing permittivity, permeability and conductivity respectively.

When coupled with the set of mechanical field equations for a deforming medium, the Lagrangian representation of Maxwell’s equations is required as a consistent platform for solving the coupled dynamic-EM initial-boundary value problem. The electromagnetic variables in Eqs. (4a)–(4d) and (5) in the reference configuration are defined in terms of current configuration variables as:

$$D_I \triangleq J X_{I,j} d_j \tag{7a}$$

$$H_J \triangleq [h_i + \varepsilon_{imn} (d_m \dot{x}_n)] x_{i,J} \tag{7b}$$

$$J_I^c \triangleq J X_{I,j} j_j^c \tag{7c}$$

$$E_I \triangleq [e_j - \varepsilon_{jmn} (b_m \dot{x}_n)] x_{j,I} \tag{7d}$$

$$B_J \triangleq J X_{J,i} b_i. \tag{7e}$$

Following a detailed derivation presented in [25], the four Maxwell’s equations in the reference configuration are written as:

$$D_{I,I} = Q_e \tag{8a}$$

$$B_{J,J} = 0 \tag{8b}$$

$$\varepsilon_{IJK} \frac{\partial}{\partial X_J} E_K = -\frac{d}{dt} B_I \tag{8c}$$

$$\varepsilon_{IJK} \frac{\partial}{\partial X_J} H_K = \frac{d}{dt} D_I + J_I^c. \tag{8d}$$

The corresponding set of constitutive relations in the reference configuration are:

Electric displacement field:  $D_I = \varepsilon J C_{IJ}^{-1} \left[ E_J + \varepsilon_{JKL} \left( \frac{\partial X_K}{\partial t} B_L \right) \right]$  (9a)

Magnetic field strength:  $H_J = \frac{1}{\mu} J^{-1} C_{MJ} B_M + \varepsilon_{JKL} \frac{\partial X_K}{\partial t} \left\{ \varepsilon J C_{LN}^{-1} \left[ E_N + \varepsilon_{NPQ} \left( \frac{\partial X_P}{\partial t} B_Q \right) \right] \right\}$  (9b)

Current:  $J_I^c = \sigma J C_{IJ}^{-1} E_J.$  (9c)

These relations are nonlinear due to coupling with the deformation fields. For efficient solution of the Maxwell’s equations, scalar and vector potentials  $\varphi$  and  $\mathbf{a}$  respectively in the current configuration have been proposed as primary variables representing the electric and magnetic fields [43]. This potential function representation results in

identities in Eqs. (4b) and (4c). The reduced forms of the Maxwell’s equations in the reference configuration require transformation of the potentials. The magnetic and electric fields can be derived in terms of the vector potential ( $\mathbf{A}$ ) and mixed potentials ( $\Phi, \mathbf{A}$ ) in the reference configuration [25] as:

$$E_I = -\Phi_{,I} - \frac{\partial A_I}{\partial t} \quad \text{and} \quad B_I = \varepsilon_{IJK} A_{K,J}. \tag{10}$$

Substituting Eqs. (10) in Eqs. (8a) and (8d) results in two governing Maxwell’s equations in a deformable medium, given as:

$$\left( \varepsilon J C_{IJ}^{-1} \tilde{E}_J \right)_{,I} = Q_e \tag{11a}$$

$$\varepsilon_{IJK} \left( \frac{1}{\mu J} C_{KLE} \varepsilon_{LMN} A_{N,M} + \varepsilon_{K PQ} \frac{\partial X_P}{\partial t} \varepsilon J C_{QR}^{-1} \tilde{E}_R \right)_{,J} = \varepsilon \frac{d}{dt} \left( J C_{IP}^{-1} \tilde{E}_P \right) + \sigma J C_{IQ}^{-1} (-\Phi_{,Q} - \dot{A}_Q) \tag{11b}$$

where  $\tilde{E}_I$  is defined as:

$$\tilde{E}_I = E_I + \varepsilon_{IJK} \frac{\partial X_J}{\partial t} B_K = -\Phi_{,I} - \dot{A}_I + \varepsilon_{IJK} \frac{\partial X_J}{\partial t} \varepsilon_{KMN} A_{N,M}. \tag{12}$$

The reduced equations in terms of potentials reduce the number of unknowns from 6 to 4 independent variables in the semi-discrete finite element model. However the potentials are non-unique and will yield singular tangent matrices with instabilities for certain electromagnetic fields. For instance non-unique solutions of the vector potential may be found in Eq. (10), for which the Gauss’s law of magnetism in Eq. (8b) still holds.

$$B_I = \varepsilon_{IJK} A_{K,J} + \Psi_{,I} \tag{13}$$

where  $A_I$  is the  $I$ -th component of the vector potential and  $\Psi$  is an arbitrary scalar potential in the reference configuration. The non-uniqueness of the potentials is averted by applying a Coulomb gauge condition [27,44,45], stated as:

$$A_{I,I} = 0. \tag{14}$$

### 3. Review of a few candidate accelerated time integration methods

For the coupled mechanical-electro-magnetic problems, two relevant time-scales that implicitly exist are:

1. A high resolution, fine time-scale  $\tau$  corresponding to the high frequency electromagnetic cycles;
2. A low resolution, coarse time-scale  $N$  corresponding to the low frequency of mechanical cycles.

A variety of accelerated time integration methodologies have been proposed in the literature for different problems e.g. [32–34,40,46]. Many of these approaches have limitations when solving nonlinear problems involving multiple time-scales, as discussed in [40,41]. In this section, a few of these methods are examined for their feasibility with the coupled transient electro-magnetic, dynamic (EM–ME) problem.

#### 3.1. Test problem: reduced Maxwell’s equations without mechanical field

A simplified test problem is considered for assessing the appropriateness of various candidate multi-time scaling schemes. Consider the Faraday’s law of magnetism and Ampere’s law in Eqs. (4c) and (4d) for linear, isotropic, nondispersive materials that have field direction and frequency independent electromagnetic properties [27,28]. Following steps in [47], a system of symmetric equations is obtained by incorporating an equivalent magnetic current density in the Faraday’s law. The structure is assumed to (a) have an infinite cross-section in the  $y - z$  plane and (b) have no variation of the electromagnetic fields in the  $y$  and  $z$  directions. If electromagnetic excitations are imposed in the  $x$ -direction only, then the partial derivatives of all fields with respect to the  $y$ - and  $z$ - coordinates are zero. Additionally the following assumptions:

$$\frac{\partial e_y}{\partial x}(t \geq 0) = 0 \quad \text{and} \quad h_z(t = 0) = 0 \implies \frac{\partial h_z}{\partial t}(t = 0) = 0 \quad \text{and} \quad h_z(t \geq 0) = 0 \tag{15a}$$

$$e_y(t = 0) = 0 \implies \frac{\partial e_y}{\partial t}(t = 0) = 0 \quad \text{and} \quad e_y(t \geq 0) = 0 \tag{15b}$$

yield a set of only two, coupled scalar equations involving  $e_z$  and  $h_y$  that correspond to a  $x$ -directed,  $z$ -polarized transverse magnetic mode, i.e.

$$\frac{\partial e_z}{\partial x} = \mu \frac{\partial h_y}{\partial t} + \sigma^* h_y \dots \text{(a)} \quad \text{and} \quad \frac{\partial h_y}{\partial x} = \epsilon \frac{\partial e_z}{\partial t} + \sigma e_z \dots \text{(b)}. \quad (16)$$

Constitutive relations for electric current density  $j_i^f = j_i^c = \sigma e_i$  and equivalent magnetic current density  $m_i = \sigma^* h_i$  in the absence of mechanical fields are used. Initial and boundary conditions for a conductor of length  $x = l$  are assumed to be:

$$\underline{\text{IC}}: e_z(x, 0) = 0 \quad \text{and} \quad h_y(x, 0) = 0 \quad \underline{\text{BC}}: e_z(l, t) = \bar{e}_z(t) \quad \text{and} \quad h_y(l, t) = \bar{h}_y(t). \quad (17)$$

The weak forms of the initial-boundary value problem in Eqs. (16) are written as:

$$\epsilon \int_l \delta e_z \dot{e}_z dx + \sigma \int_l \delta e_z e_z dx - \int_l \delta e_z h_{y,x} dx = 0 \quad (18a)$$

$$\mu \int_l \delta h_y \dot{h}_y dx + \sigma^* \int_l \delta h_y h_y dx - \int_l \delta h_y e_{z,x} dx = 0 \quad (18b)$$

where  $\delta e_z$  and  $\delta h_y$  are virtual test functions with properties that  $\delta e_z = 0$  and  $\delta h_y = 0$  on the essential boundary. The Newmark-beta time integration method is implemented to incrementally solve Eqs. (18). For cyclic loading, the solution requires a large number of very small time steps in each electromagnetic cycle.

The Eqs. (18) are solved for the domain of length  $l = 0.003$  m discretized into 100 linear elements. Material properties are: electrical permittivity  $\epsilon = 7.0832 \times 10^{-11}$  F/m, magnetic permeability  $\mu = 1.2567 \times 10^{-6}$  H/m, electrical conductivity  $\sigma = 2.5 \times 10^6$  S/m and  $\sigma^* = 2.5 \times 10^6$   $\Omega$ /m. The electrical current excitation is imposed at the end  $x = l$  and assumed to be a periodic signal with an arbitrary oscillatory pattern as  $\bar{e}_z(t) = f(\omega_{em}t)$  with  $\omega_{em} = 200\pi$  (rad/s). Electromagnetic field variables at  $t = 0$  are assumed to be zero. The simulation is continued for 1000 electrical cycles using a single time-scale Newmark-beta integration method.

The results of the  $z$ -direction electric field and  $y$ -direction magnetic field as a function of the cycles, at the midpoint of the conductor  $(\frac{l}{2}, 0, 0)$  are plotted in Fig. 1. The figures in the inset correspond to the oscillatory response of the electric and magnetic fields at the 151-th cycle. These constitute the reference response solutions for validating candidate methods that are discussed in the following sections. A cycle dependent least square error at a nodal point  $\beta$ , accounting for the values of the electric field at the beginning of each cycle, is defined as:

$$er^\beta(N) = \frac{\left[ \sum_{N=1}^{N_{\max}} \left( e_z^\beta(NT) - e_{z(ref)}^\beta(NT) \right)^2 \right]^{\frac{1}{2}}}{\left[ \sum_{N=1}^{N_{\max}} \left( e_{z(ref)}^\beta(NT) \right)^2 \right]^{\frac{1}{2}}} \quad (19)$$

where  $N$  and  $N_{\max}$  are the number of electromagnetic cycles and its maximum value,  $T$  is the period and the subscript  $ref$  corresponds to the single time-scale solution.

### 3.2. Exponential Runge–Kutta adaptive stepping

The Runge–Kutta exponential time discretization methods, which have good stability properties for dissipative PDEs and nonlinear wave equations [35–39], are applied to solve the problems in Section 3.1. These methods involve integration of the governing equations using exponential time differencing scheme, followed by an approximation of the integrals involving the nonlinear constitutive relations and loading functions using Runge–Kutta family of methods. The solution consists of two parts, viz. a fast phase and a slow manifold. Initial conditions are not satisfied for the slow phase expansions. Hence a cycle by cycle integration is required to guarantee the stability of the scheme. The optimal step size  $h_{opt}$  is obtained from a local truncation error meeting an assigned tolerance [39]. The electric field at the beginning of each cycle  $e_z^0$  is plotted as a function of the cycles for different accelerated time integration schemes in Fig. 2(a). This method yields accurate results for an increment size  $h_{opt} = 4\Delta t_{sts}$ , where  $\Delta t_{sts}$  is the time-step of a conventional single time-scale integration process with twice the efficiency. Fig. 2(b) shows the speedup with

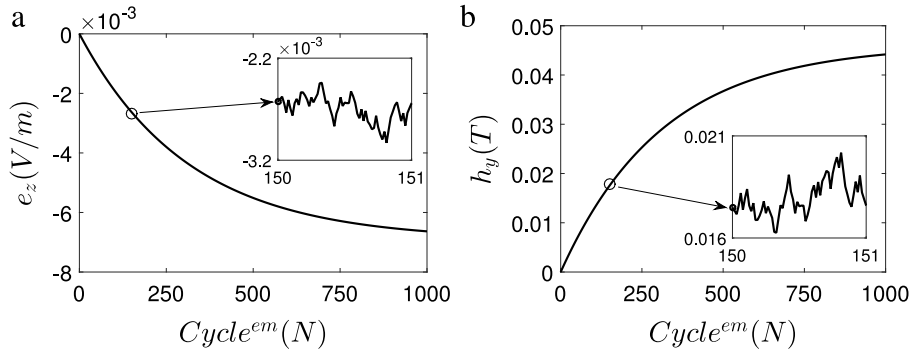


Fig. 1. Reference solutions for the problem with applied arbitrary periodic current excitation: (a) electric field component  $e_z$  and (b) magnetic field component  $h_y$ , obtained by a single-scale time integration scheme. Figures in the boxed inset correspond to blown up response within a single cycle interval.

each accelerated method over the single time-scale Newmark-beta method, as a function of the error in Eq. (19). For the Runge–Kutta (RK4) method, a small advantage in the efficiency leads to high truncation error.

### 3.3. Asymptotic and almost periodic homogenization methods

Methods of multi-time scaling using uniformly varying asymptotic solutions have been discussed for only Maxwell’s equations in [30,31]. These methods are based on the existence of two temporal scales, viz a macro time-scale ( $t$ ) and a micro time-scale ( $\tau$ ), linked through a relation  $t = \tau \zeta$  for  $0 < \zeta \ll 1$ . In general, they assume complete scale-separation and invoke homogenization method that requires solution of the fine time-scale ( $\tau$ ) initial value problem in each coarse time-step. This results in high computational efforts that will not provide any advantage over the single time-scale calculations. Additionally, the assumptions of scale-separation through periodicity can lead to large errors for general multi-physics problems. Attempts to overcome this limitation through interpolation-based hierarchical modeling in [32] have not resulted in favorable results for history dependent problems. An advancement over the asymptotic homogenization has been suggested through the almost-periodic temporal homogenization (APTH) operator in [33,34] for studying fatigue response. The initial–boundary value problem is decomposed into macro-scale evolution equations and the micro-scale temporal problems for different orders of the scaling function  $\zeta$ . The equations are solved using a staggered, modified Euler time integration scheme. The macro-scale variables at time  $t_{n+1}$  are updated and then micro-scale initial–boundary value problems are solved with the updated values of the macro-scale variables in the time domain  $[0, \tau]$ . In its application to the electromagnetic problems, the initial conditions for the macro-scale and micro-scale equations are obtained by solving one electromagnetic cycle using a single time scale integration scheme, as the starting procedure. This method leads to truncation error in the macro time steps  $\Delta t$  and consequently imposes very small time steps in the macro scale equations to preserve numerical stability. This is illustrated in Fig. 2(a) where it shows oscillations with a step-size of four cycles or higher, i.e.  $\Delta N \geq 4$ . The efficiency as a function of accuracy is shown in Fig. 2(b). When compounded with nonlinearities due to coupling with the mechanical fields, the efficiency of the APTH method is expected to reduce drastically.

### 3.4. Discrete Fourier transforms

Fourier transforms can be used for accelerated solution of the reduced set of Maxwell’s equations in Eq. (18). The Fourier transform generalizes the complex Fourier series to accommodate non-periodic functions through an integral expression using exponential basis functions over a time period  $T \rightarrow +\infty$ , given as:

$$\mathbf{v}_k(\mathbf{x}) = \mathbf{v}(\mathbf{x}, k) = \lim_{T \rightarrow \infty} \int_{-\frac{T}{2}}^{\frac{T}{2}} \mathbf{v}(\mathbf{x}, t) e^{-\frac{i2\pi kt}{T}} dt \quad \text{where } \mathbf{v}(\mathbf{x}, k) = \begin{Bmatrix} \mathbf{e}(\mathbf{x}, k) \\ \mathbf{h}(\mathbf{x}, k) \end{Bmatrix} \quad (20)$$

where  $k$  is an integer variable corresponding to the number of harmonics in the transformation with points in the frequency spectrum that are spaced  $1/T$  apart, and  $\{\mathbf{e}, \mathbf{h}\}$  are the electric and magnetic fields respectively. With

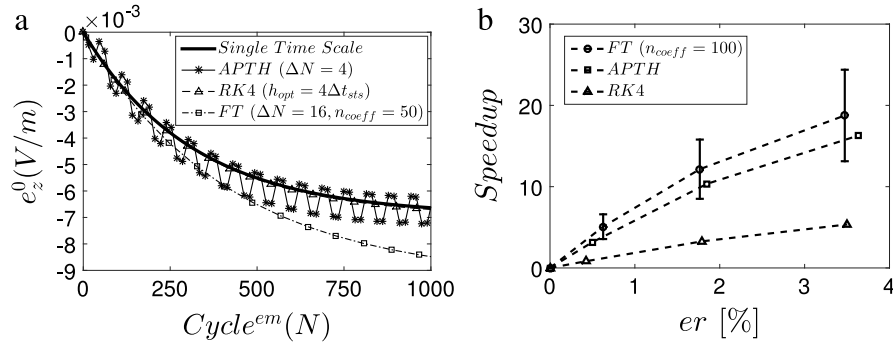


Fig. 2. Comparison of accuracy and efficiency of various accelerated time integration methods with the single time scale integration scheme: (a) electric field component  $e_z^0$  as a function of cycles and (b) speedup over the single time-scale method as a function of the error in the electric field.

$T \rightarrow +\infty$ , this transformation approaches a continuous frequency domain. The transformation bases are functions of the characteristic angular frequency  $\omega_k = \frac{2\pi k}{T}$  that capture the heterogeneous oscillations within an interval  $T$ . In the discrete Fourier transformation scheme, the integral in Eq. (20) is expressed as a summation over equally spaced discrete points in the frequency spectrum. Accordingly the Fourier coefficients in Eq. (20) can be obtained by replacing the Fourier integral with a Riemann sum [48,49]. For solving the test Maxwell's boundary value problem,  $T$  is chosen to be the time period of the electrical current excitation i.e.  $T = \frac{2\pi}{\omega_{em}}$ , which remains constant with progressing cycles.

A dual time-scale representation  $t = NT + \tau$ , with  $N$  representing the electromagnetic cycles and  $\tau \in [0, T]$  representing the intra-cycle time-scale is used. For a given cycle  $N$ , the limits of integration in Eq. (20) are changed to  $[NT, (N+1)T]$  to correspond to the discrete Fourier transformation of the state variables e.g.  $\{\mathbf{e}, \mathbf{h}\}$ . Within this time interval for the periodic basis functions, the variable  $t$  can be replaced by  $\tau$  in the integral. Transformation of the state variables  $\{\tilde{\mathbf{v}}^\beta(N, \tau)\} = \{\dot{e}_z^\beta(N, \tau), \dot{h}_y^\beta(N, \tau)\}$  leads to the discrete Fourier coefficients:

$$\begin{aligned} \tilde{c}_k^\beta(N) &= \frac{1}{\sqrt{n}} \sum_{j=0}^{n-1} \dot{e}_z^\beta(N, \tau_j) e^{(-i2\pi\tau_j k)} \\ \tilde{d}_k^\beta(N) &= \frac{1}{\sqrt{n}} \sum_{j=0}^{n-1} \dot{h}_y^\beta(N, \tau_j) e^{(-i2\pi\tau_j k)} \quad \forall k = 0, \dots, n-1 \end{aligned} \quad (21)$$

where  $n$  is the required number of basis functions for accurate representation of the oscillatory response of  $\{\mathbf{v}^\beta\}$  within a cycle. The equally spaced sample points are defined as  $\tau_j = \frac{(j+1)T}{n}$  for  $j = 0, \dots, n-1$ . This procedure transforms the time dependent boundary value problem into a cycle-scale  $N$  boundary value problem termed as the coarse time-scale problem. Upon solving this problem for the coefficients in Eq. (21), the fine  $\tau$ -scale electromagnetic fields can be recovered from the inverse transformation of Eq. (21). The initial and boundary conditions for the boundary value problem in Eqs. (17) can then be reformulated as:

$$\underline{\text{IC:}} \quad e_z^0(x, N=2) = e_z^{ref}(x, t=T) \quad \text{and} \quad h_y^0(x, N=2) = h_y^{ref}(x, t=T) \quad (22a)$$

$$\begin{aligned} \underline{\text{BC:}} \quad \tilde{c}_k(l, N) &= \frac{1}{\sqrt{n}} \sum_{j=0}^{n-1} \frac{\partial \tilde{e}_z(N, \tau_j)}{\partial t} e^{(-i2\pi\tau_j k)} \quad \text{and} \\ \tilde{d}_k(l, N) &= \frac{1}{\sqrt{n}} \sum_{j=0}^{n-1} \frac{\partial \tilde{h}_y(N, \tau_j)}{\partial t} e^{(-i2\pi\tau_j k)}. \end{aligned} \quad (22b)$$

By substituting the inverse transform of Eqs. (21) and applying the initial and boundary conditions in Eqs. (22a) and (22b), the semi-discrete finite element equations (18) are now obtained in terms of discrete Fourier coefficients  $\{\mathbf{c}^\beta(N), \mathbf{d}^\beta(N)\}$ . By inverse transformation of Eq. (21) and integrating over a cycle by assigning  $j = n$  or  $\tau_j = T$ ,

the coarse “cycle”-scale derivatives of the state variables are obtained as:

$$\frac{de_z^{0\beta}}{dN} = e_z^\beta(N, T) - e_z^{0\beta}(N) = \frac{T}{i2\pi\sqrt{n}} \sum_{k=0}^{n-1} \frac{\tilde{c}_k^\beta(N)}{k} \tag{23a}$$

$$\frac{dh_y^{0\beta}}{dN} = h_y^\beta(N, T) - h_y^{0\beta}(N) = \frac{T}{i2\pi\sqrt{n}} \sum_{k=0}^{n-1} \frac{\tilde{d}_k^\beta(N)}{k} \tag{23b}$$

where  $e_z^{0\beta}(N) = e_z^\beta(N, 0)$  and  $h_y^{0\beta}(N) = h_y^\beta(N, 0)$ . The above equations, relating the evolution of the cycle-scale state variables through the constitutive laws, can be integrated with using any time integration algorithm. A multi-step, second order backward Euler time integration algorithm is used, where the Fourier coefficients in the  $\tau$  scale are used for convergence.

The cycle-scale Eqs. (23a) and (23b) obtained through Fourier transformation of the boundary value problem in Eq. (18) results in accurate solutions for a harmonic electrical excitation. The discrete Fourier coefficients in Eqs. (21) are exact with this excitation for representing the fine time-scale state variables. The second order backward Euler time integration algorithm is stable and the cycle-scale equations can be integrated with large time steps without loss of accuracy or spurious oscillations in the response functions. However for non-harmonic signals, such as the one considered for the test problem, finite terms ( $n \ll \infty$ ) in the summations of Eq. (21) lead to a lack of uniform converge due to Gibbs instability. This is shown with the high truncation error in Fig. 2(a), where the solution process uses  $\Delta N = 16$ ,  $n_{coeff} = 50$  and  $n = 256$ . A non-harmonic signal is being represented here through a finite number of exponential basis functions in the discrete Fourier transform. The deviation of the Fourier transform-based solution from the reference solution keeps increasing with cycles, due to increasing truncation error in the fine time-scale reconstruction. The corresponding accuracy and efficiency is illustrated in Fig. 2(b). Error bars, corresponding to the standard deviation of the efficiency with different number of Fourier coefficients, are shown in this figure. Additional terms in the basis and coefficients result in higher accuracy. To summarize, the spectral basis representation in the Fourier transform leads to Gibbs type instabilities in the response solution due to truncation of terms from the infinite set of Fourier coefficients. The periodic nature of these basis functions makes them inappropriate for representing non-periodic fine scale oscillations.

These studies conclude that most of the conventional methods of time acceleration are not adequate even for the uncoupled electro-magnetic problem. Convergence issues, with respect to both accuracy and efficiency, are expected to deteriorate for the coupled multi-physics problem that is central to this development.

#### 4. Wavelet transforms in multi-time scaling

For the class of coupled oscillatory problems being modeled in this study, the family of basis functions chosen for any accelerated time-scaling algorithm should ideally meet the following criteria.

- Functions should be linearly independent and form an orthogonal set to satisfy the condition:  $\frac{1}{T} \int_0^T \psi_k \psi_l d\tau = \delta_{kl}$ ;
- Functions should represent all possible waveforms to a predefined resolution;
- The number of coefficients, corresponding to the number of basis functions must be optimally small.

Wavelet transformation induced multi-time scaling (WATMUS) methods have been successfully implemented in [40–42] to simulate a large number of loading cycles for fatigue life prediction in polycrystalline microstructures. Analogously, the wavelet family of transformation functions is considered to be a strong candidate for introducing multi-time scaling to multi-physics problems governed by disparate frequency domains. Many wavelet basis functions possess the following properties that make them favorable for this class of problems.

- *Compact support*: Each wavelet basis has a compact support, spanning a finite domain. Consequently, wavelet-based solutions are not expected to exhibit spurious instabilities due to cut-off, like the Gibbs phenomena.
- *Multi-resolution*: For a given resolution of the fine-scale response, the space of basis functions is well defined and finite, which makes it possible to a-priori identify wavelet basis functions to represent the oscillatory fine-scale variables.
- *Number of coefficients*: Since wavelet transformation projects in both time and frequency domains unlike Fourier transform, it enables a significantly larger reduction in the number of coefficients to be solved.

- *Non-periodic bases:* Wavelet basis functions are non-periodic and suitable for accurate representation of non-periodic oscillatory response.

#### 4.1. Overview of wavelet basis functions

Wavelet basis functions evolve from the translation and dilation of compactly supported scaling functions  $\phi(\tau)$  and mother wavelets  $\psi(\tau)$  [50,51]. The dilation property provides multi-resolution characteristic needed for accurately representing complex waveforms, while the translation property provides representation across a range of multiple periods. The wavelet transformation-based representation of any square integrable function  $v(\tau)$  is:

$$v(\tau) = \sum_{m=1}^{M_{res}} \sum_{n=1}^{N_{trans}^m} \hat{C}_{m,n} 2^{\frac{m}{2}} \psi(2^m \tau - n) \tag{24}$$

where  $\hat{C}_{m,n} = \int_{-\infty}^{\infty} v(\tau) 2^{-\frac{m}{2}} \psi(2^m \tau - n) d\tau$  are coefficients of the wavelet basis functions expressed as a vector,  $M_{res}$  is the number of dilation modes of resolution and  $N_{trans}^m$  is the number of translation modes corresponding to each resolution  $m$ . The compactly supported scaling functions  $\phi(\tau)$  satisfy the refinement condition, which relates the higher and lower resolution scaling functions through a recursive summation and multiplication of the high pass filter components  $h_k$  as:

$$\phi(\tau) = \sum_{k=1}^{N_{filter}} h_k \phi(2\tau - k) \tag{25}$$

where the coefficients  $h_k$  correspond to a high pass filter and  $N_{filter}$  is a parameter corresponding to the total number of filters for the wavelet family. Scaling functions produce a nested sequence of subspaces at different resolutions, expressed as:

$$0 \subset \dots \subset V_0 \subset V_1 \subset \dots \subset V_m \subset V_{m+1} \subset \dots \subset L^2(R). \tag{26}$$

The nested sequence of functions  $v_m$ , obtained by projecting  $v$  to the different subspaces  $V_m$ , are the approximations at different resolution levels. This multi-resolution property yields a complimentary detail space  $W_m$  that is spanned by the wavelet basis functions  $\psi(\tau)$ .  $W_m$  constitutes a space corresponding to the orthogonal projection of  $V_{m+1}$  on  $V_m$ , i.e.  $V_{m+1} = V_m \oplus W_m$ . Wavelet basis functions have compact support and satisfy refinement condition similar to the scaling functions, as:

$$\psi(\tau) = \sum_{k=1}^{N_{filter}} g_k \phi(2\tau - k) \tag{27}$$

where  $g_k$  are coefficients corresponding to a low pass filter that depend on the family of wavelets. Scaling and mother wavelet functions for a candidate Daubechies-8 wavelet family [52,53] over its support length are shown in Fig. 3.

Discrete wavelet transformation may be achieved through a recursive projection of the original function on to the approximate and detail spaces at coarser resolutions as:

$$\begin{aligned} v^m(\tau) &= \sum_n \langle v^m, \phi_{m-1,n} \rangle \phi_{m-1,n} + \sum_n \langle v^m, \psi_{m-1,n} \rangle \psi_{m-1,n} \\ &= \sum_n a^{m-1,n} \phi_{m-1,n} + \sum_n d^{m-1,n} \psi_{m-1,n} = v^{m-1} + \sum_n d^{m-1,n} \psi_{m-1,n} \end{aligned} \tag{28}$$

where  $m$  is the resolution level and  $n$  is the translation at the corresponding resolution. It yields approximate coefficients  $a^{1,n} \in V_0$  and detail coefficients  $d^{m,n} \in W_m$  where  $m \in [1, M_{res}]$ . This multi-resolution property of wavelet transformation may be used to retain coefficients, where response variations are high and eliminate coefficients where changes are slow. Discrete wavelet transformation of Eq. (28) can be performed through a matrix operation:

$$\mathbf{C} = \mathbf{T}\mathbf{v} \tag{29}$$

where the transformation matrix  $\mathbf{T}$  is orthogonal and sparse. It is created from low pass filters  $h_k$  and high pass filters  $g_k$  as discussed in [40,42,51].  $\mathbf{v}$  is a  $p$ -dimensional vector containing  $p$  equally spaced discrete points in time.  $\mathbf{C}$  is a

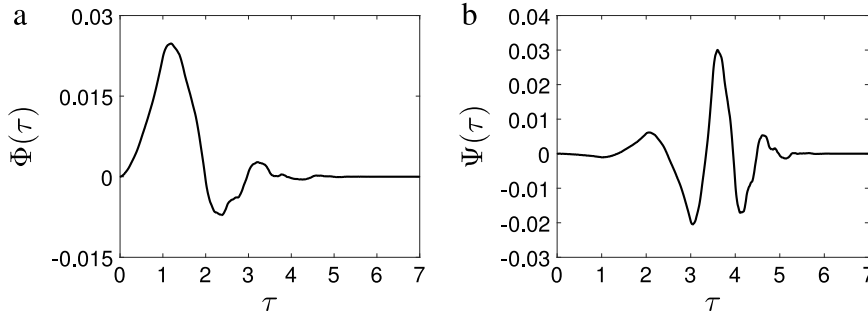


Fig. 3. (a) Daubechies-8 scaling function  $\phi$ , and (b) Daubechies-8 wavelet function  $\psi$ .

$q$ -dimensional vector that contains the wavelet coefficients corresponding to both dilation and translation. Depending on the signal  $\mathbf{v}$  and the compactly supported wavelet basis functions, there can be only  $q \leq p$  non-zero coefficients. The vector of non-zero coefficients can be mapped to the signal through the transformation matrix  $\tilde{\mathbf{T}}$ , which is constructed from the columns of  $\mathbf{T}^T$  corresponding to non-zero coefficients of  $\mathbf{C}$ , as:

$$\tilde{T}_{jk} = T_{ij} \quad \text{for } C_i \neq 0 \text{ where } k = 1, \dots, q \text{ and } i, j = 1, \dots, p. \tag{30}$$

For a properly chosen family of wavelet basis functions corresponding to a given signal, the above representation using a rectangular transformation matrix  $\tilde{\mathbf{T}}$  significantly reduces the computational requirements for fine time scale decomposition and reconstruction to a predefined resolution.

#### 4.2. Accelerated FE solution of the reduced Maxwell’s IBVP using the WATMUS algorithm

The same test problem of Section 3 is solved with the WATMUS algorithm developed here for the multi-physics problem. The wavelet transformation is used to resolve the response of an arbitrary oscillatory field variable at time  $t$  into components characterized by: (i) a slowly evolving response, corresponding to wavelet coefficients that evolve in the cycle scale  $N$ , and (ii) a rapidly varying oscillatory response represented by the intra-cycle,  $\tau$ -scale wavelet basis functions. Let the elapsed time  $t = \sum_i^N T_i + \tau$ , where  $T_i$  corresponds to the period of the  $i$ -th cycle. Note that the  $T_i$ ’s will be different for non-periodic response. Any field variable  $v(\mathbf{x}, t)$  may be expanded in a series of  $n$  wavelet basis functions as:

$$v(\mathbf{x}, t) = v(\mathbf{x}, N, \tau) = \sum_{k=1}^n v_k(\mathbf{x}, N) \psi_k(\tau) \quad \forall \tau \in \left[ \sum_i^N T_i, \sum_i^{N+1} T_i \right] \tag{31}$$

where  $v_k(\mathbf{x}, N)$  are the cycle-scale coefficients, corresponding to the wavelet basis functions  $\psi_k(\tau)$ . For convenience,  $v^0(\mathbf{x}, N) = v(\mathbf{x}, N, 0)$  at the beginning of a given cycle is identified as a coarse-scale variable. For the cycle-scale problem, the wavelet transformation is applied to eliminate the fine time-scale dependencies and yield a discrete evolution equation of the canonical form:

$$v^0(\mathbf{x}, N + \Delta N) = f(\mathbf{x}, N, v^0(\mathbf{x}, N), v_k(\mathbf{x}, N)). \tag{32}$$

The wavelet coefficients  $v_k(\mathbf{x}, N)$  are determined by taking the inner product of the response function with the orthogonal wavelet basis functions over the interval  $[\sum_i^N T_i, \sum_i^{N+1} T_i]$  as:

$$v_k(\mathbf{x}, N) = \frac{1}{T} \int_{\sum_i^N T_i}^{\sum_i^{N+1} T_i} v(\mathbf{x}, N, \tau) \psi_k(\tau) d\tau \quad \text{where } k = 1, \dots, n. \tag{33}$$

For the test problem of reduced Maxwell’s equations, the response function corresponds to the set  $v(\mathbf{x}, N, \tau) = [\dot{e}_z^\beta(\mathbf{x}, N, \tau), \dot{h}_y^\beta(\mathbf{x}, N, \tau)]$ , with  $v_k(\mathbf{x}, N)$  being the wavelet coefficients. Correspondingly, the discrete wavelet transformation of Eq. (33) is performed through the matrix operations in Section 4.1 as:

$$\tilde{e}_k^\beta(N) = \tilde{T}_{jk}^\beta \dot{e}_z^\beta(N, \tau_j) \quad \text{and} \quad \tilde{d}_k^\beta(N) = \tilde{T}_{jk}^\beta \dot{h}_y^\beta(N, \tau_j) \tag{34}$$

where  $\tilde{T}_{ij}^\beta$  represents the orthonormal transformation matrix, (i.e.  $\tilde{\mathbf{T}}^\beta \tilde{\mathbf{T}}^{\beta T} = \mathbf{I}$ ) created from the wavelet filter. The electromagnetic field variables are obtained by integrating the transpose of discrete equations (34) as:

$$e_z^\beta(N, \tau_j) = e_z^{0\beta}(N) + \left( \int_0^{\tau_j} \tilde{T}_{jk}^\beta(\tau) d\tau \right) \tilde{c}_k^\beta(N) \quad (35a)$$

$$h_y^\beta(N, \tau_j) = h_y^{0\beta}(N) + \left( \int_0^{\tau_j} \tilde{T}_{jk}^\beta(\tau) d\tau \right) \tilde{d}_k^\beta(N). \quad (35b)$$

The starting procedure of the WATMUS requires solving the first cycle  $N = 1$  in detail using the single time-scale integration process. The boundary and initial conditions in (17) are then expressed as:

$$\text{IC: } e_z^0(x, N = 2) = e_z^{ref}(x, t = T) \quad \text{and} \quad h_y^0(x, N = 2) = h_y^{ref}(x, t = T) \quad (36a)$$

$$\text{BC: } \tilde{c}_k(l, N) = \tilde{T}_{jk} \frac{\partial \tilde{e}_z(N, \tau_j)}{\partial t} \quad \text{and} \quad \tilde{d}_k(l, N) = \tilde{T}_{jk} \frac{\partial \tilde{h}_y(N, \tau_j)}{\partial t}. \quad (36b)$$

Here, the superscript *ref* corresponds to the single time-scale solution at the end of the first cycle. By substituting Eqs. (35a) and (35b) and the transpose of Eqs. (34), the semi-discrete finite element equations (18) are expressed in terms of discrete wavelet coefficients. The coarse time scale evolution equations are obtained by setting  $\tau_j = T$  in Eqs. (35a) and (35b) to yield:

$$\frac{de_z^{0\beta}}{dN} = e_z^\beta(N, T) - e_z^{0\beta}(N) = \left( \int_0^T \tilde{T}_{jk}^\beta(\tau) d\tau \right) \tilde{c}_k^\beta(N) \quad (37a)$$

$$\frac{dh_y^{0\beta}}{dN} = h_y^\beta(N, T) - h_y^{0\beta}(N) = \left( \int_0^T \tilde{T}_{jk}^\beta(\tau) d\tau \right) \tilde{d}_k^\beta(N). \quad (37b)$$

These cycle-scale equations are integrated with a stable, 2nd-order backward Euler time integration scheme.

Table 1 compares the effect of three different wavelet families in terms of efficiency and accuracy of the solution to the test Maxwell's problem undergoing non-periodic excitation. Wavelet families considered are: (i) Daubechies-8 (Db8), (ii) Symlets-3 (Sym3) and (iii) Biorthogonal-39 (Bior39), as given in [53]. Solutions are compared for different tolerances ( $\eta(c_k^\beta, d_k^\beta)$ ) in the iteration algorithm, number of wavelet coefficients ( $n_{wav}$ ) and cycle-step sizes ( $\Delta N$ ). The fine time-scale error in Eq. (19) is used for comparing the accuracy of the simulations. Speedup in the table corresponds to the ratio of the CPU time required by the WATMUS scheme with that by the single time-scale simulation. The Biorthogonal-39 family shows a high error in the fine time-scale reconstruction, of the same order as the discrete Fourier transform. The results are significantly improved with the Daubechies-8 and Symlets-3 wavelets, with the former performing a little better than the latter. Consequently, Daubechies-8 is used as the wavelet basis of choice in the WATMUS scheme for solving the coupled boundary value problem. An unconditionally stable time integration method for the cycle-scale equations (37a) and (37b) yields accurate solutions without spurious oscillations. For the simulations, eight resolutions, i.e.  $M_{res} = 8$  corresponding to  $n_{wav} = 256$  are used. The optimal number of wavelet coefficients, based on a tolerance  $\eta(c_k^\beta, d_k^\beta) = 10^{-4}$  is obtained as 50. The speedup for step sizes  $\Delta N = 16, 128$  and  $500$  are  $24, 85$  and  $111$  respectively. The fine time-scale error at  $N = 963$  is shown in Fig. 4(a) and (b) respectively. The truncation error quickly converges to very low values with increasing number of wavelet coefficients. Also relatively high accuracy can be achieved with relatively high values of  $\Delta N$ . These studies confirm the potential of the WATMUS method for the coupled multi-physics problems. This is extended to the 3D coupled electromagnetic nonlinear dynamic FE model with the adaptivity criteria in the next section.

## 5. The WATMUS method for 3D coupled electromagnetics-nonlinear dynamical FE model

The initial-boundary value problem for the coupled, transient electromagnetics-nonlinear dynamical problem is governed by:

- Equations of equilibrium for large deformation, nonlinear dynamic problem, which in the reference configuration is given in Eq. (3);

- Transient equilibrium conditions for the electromagnetic potentials, which in the reference configuration are expressed in Eqs. (11a) and (11b).

The weak form of the nonlinear dynamical equations, corresponding to the strong form in Eq. (3) is given as:

$$\int_{V_0} \delta u_i \rho_0 \ddot{u}_i dV + \int_{V_0} \delta u_{i,J} P_{iJ} dV - \int_{V_0} \delta u_i \rho_0 b_i dV - \int_{S_{0,T}} \delta u_i P_{iJ} N_J dS = 0 \quad (38)$$

where  $\delta u_i$  are test functions such that  $\delta u_i = 0$  on the surface  $S_{0,u}$ , where the essential conditions are prescribed.  $N_J$  are components of the surface normal, on which natural boundary conditions are applied. The corresponding semi-discrete finite element equation is given as:

$$\sum_e \int_{V_{0,e}} Q^\alpha \rho_0 Q^\beta \ddot{u}_i^\beta dV + \sum_e \int_{V_{0,e}} \frac{\partial Q^\alpha}{\partial X_J} P_{iJ} dV - \sum_e \int_{V_{0,e}} Q^\alpha \rho_0 b_i dV - \sum_{S_{0,T}} \int_{S_0} Q^\alpha P_{iJ} N_J dS = 0 \quad (39)$$

where  $Q^\alpha(\mathbf{X})$  are the polynomial shape functions in a reference configuration ( $\mathbf{X}$ ) element  $e$  for which  $\alpha$  corresponds to the element node numbers. The weak form of the transient EM problem is derived from the Hamilton’s principle that minimizes the action functional, defined in terms of the Lagrangian density  $\mathcal{L}$ . This is expressed in terms of the

Table 1

Comparison of accuracy and efficiency for various wavelet families: step size  $\Delta N$ , number of wavelet coefficients  $n_{wav}$ , as well as error and speedup by the WATMUS scheme for a total number of simulation cycles  $N = 963$ .

$\eta(c_k^\beta, d_k^\beta)$	$n_{wav}$	$\Delta N$	$\left\  \frac{e_z^\beta(N, \tau=1, \dots, n) - e_z^\beta(exact)(N, \tau=1, \dots, n)}{e_z^\beta(exact)(N, \tau=1, \dots, n)} \right\ $ (%)			Speedup		
			Db8	Sym3	Bior39	Db8	Sym3	Bior39
$10^{-10}$	256	16	0.0064	0.0089	0.0097	19	20	21
$10^{-10}$	256	64	0.0223	0.0598	0.0664	52	54	55
$10^{-10}$	256	128	0.1960	0.1770	0.1798	69	71	72
$10^{-10}$	256	250	1.3000	4.2817	3.6529	84	86	87
$10^{-10}$	256	500	7.1172	7.3314	8.0265	93	95	97
$10^{-7}$	100	16	0.1086	0.8630	2.3649	23	23	25
$10^{-7}$	100	64	0.3543	0.4916	2.2498	60	60	63
$10^{-7}$	100	128	0.4557	0.6466	6.4050	78	78	80
$10^{-7}$	100	250	1.6036	7.6256	10.433	95	95	96
$10^{-7}$	100	500	7.3314	8.4669	10.255	105	103	105
$10^{-4}$	50	16	0.2515	0.4075	20.668	24	24	24
$10^{-4}$	50	64	0.6107	0.6273	24.669	65	64	66
$10^{-4}$	50	128	0.7802	0.6469	30.939	85	85	87
$10^{-4}$	50	250	2.7307	8.6728	29.491	102	102	104
$10^{-4}$	50	500	8.9375	8.7224	29.314	111	110	112

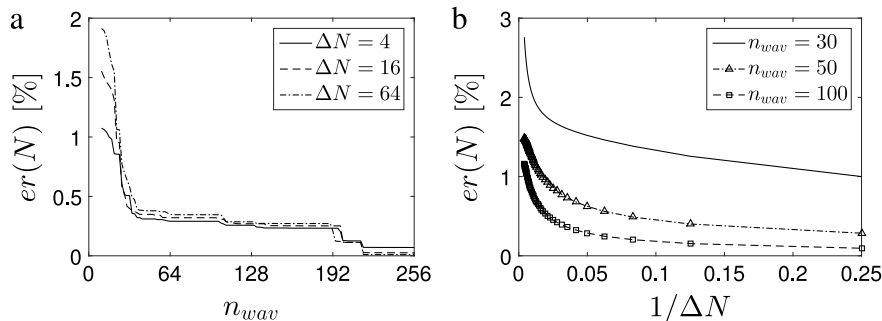


Fig. 4. Error in the  $e_z$  obtained by the WATMUS method with respect to the single time-scale integration scheme, as a function of (a) number of wavelet coefficients for different families and (b) inverse of the cycle steps at  $N = 963$ .

scalar and vector potentials in the reference configuration as:

$$\mathcal{L} = \frac{\varepsilon J}{2} C_{JK}^{-1} \tilde{E}_J \tilde{E}_K - \frac{J^{-1}}{2\mu} (C_{LM} B_L B_M) + J_N A_N - Q \Phi + \frac{1}{p} (A_{P,P})^2. \quad (40)$$

The gauge condition in Eq. (14) is implemented in Eq. (40) using the penalty constraint to the vector potentials. The term  $\frac{1}{p}$  is the penalty coefficient, where  $p$  is generally of the order of the electrical permittivity  $\varepsilon$ . Setting the variation of the action functional with respect to  $\Phi$  and  $\mathbf{A}$  to zero yields:

$$\int_{\Omega_0} \mathcal{L}_{,\Phi} [\delta \Phi] dV_0 = \int_{\partial \Omega_0} N_I (\varepsilon J C_{IJ}^{-1} \tilde{E}_J \delta \Phi) dS_0 - \int_{\Omega_0} (\varepsilon J C_{IJ}^{-1} \tilde{E}_J - \Phi) \delta \Phi_{,I} dV_0 = 0 \quad (41a)$$

$$\begin{aligned} \int_{\Omega_0} \mathcal{L}_{,\mathbf{A}} [\delta \mathbf{A}] dV_0 &= \int_{\partial \Omega_0} N_L (\varepsilon_{KLM} Q_M \delta A_K) dS_0 - \frac{2}{p} \int_{\partial \Omega_0} A_{R,R} N_K \delta A_K dS_0 \\ &+ \int_{\Omega_0} \varepsilon_{SPR} Q_P \frac{\partial}{\partial X_R} \delta A_S dV_0 - \int_{\Omega_0} \frac{d}{dt} \varepsilon J C_{KJ}^{-1} \tilde{E}_J \delta A_K dV_0 - \int_{\Omega_0} \sigma J C_{KI}^{-1} E_I \delta A_K dV_0 \\ &+ \frac{2}{p} \int_{\Omega_0} A_{R,R} \delta A_{K,K} dV_0 = 0 \end{aligned} \quad (41b)$$

with

$$Q_M = \frac{1}{\mu J} C_{MN} B_N + \varepsilon_{MNP} \frac{\partial X_N}{\partial t} \varepsilon J C_{PQ}^{-1} \tilde{E}_Q \quad (42)$$

where  $\delta \Phi$  and  $\delta \mathbf{A}$  are test functions such that  $\delta \Phi = 0$  on  $S_\Phi$  and  $\delta \mathbf{A} = \mathbf{0}$  on  $S_A$  respectively. Natural boundary conditions for  $\Phi$  or  $\mathbf{A}$  are prescribed on the surface with normal  $\mathbf{N}$ . Boundary conditions for the electromagnetic problem are given in Appendix A. The corresponding semi-discrete finite element equations incorporate the discretized scalar potential  $\Phi^\beta$  and vector potentials  $\mathbf{A}^\beta$  as independent variables.

For the single time-scale coupled problem, numerical implementation of the weak forms and boundary conditions has been conducted in [25] using a staggered approach, where the displacement field is solved first from the dynamic field equations, followed by the electromagnetic problem in every time increment. Both the mechanical and electromagnetic field variables adopt the same finite element mesh of eight-noded hexahedral elements. The implicit Newmark-beta method is implemented for integrating the dynamic problem, while the backward Euler method is implemented for integrating the EM fields.

### 5.1. Example illustrating the need for multi-time scaling in coupled EM–ME simulations

This example is intended to establish the need for multi-time scaling accompanying coupled EM–ME simulations. It simulates the evolution of a time-dependent electromagnetic field due to an alternating current in a vibrating rectangular conductor, as depicted in Fig. 5. For the mechanical problem, the boundary conditions are:  $\mathbf{u}(\mathbf{X}, t) = \mathbf{0}$  on the surface  $S_2$  and  $u_z(\mathbf{X}, t) = u_0 \sin(\omega_{me} t)$  on the surface  $S_1$ , while the initial conditions are:  $\mathbf{u}(\mathbf{X}, 0) = \dot{\mathbf{u}}(\mathbf{X}, 0) = \mathbf{0}$ . For the electromagnetic problem, the Dirichlet boundary condition is chosen to constrain the magnetic potential on all the lateral surfaces, i.e.  $\mathbf{A}(\mathbf{X}, t) = \mathbf{0}$  on all  $S \cap (S_1 \cup S_2)$ . A Neumann boundary condition is imposed in terms of the electrical current  $J_y(t) = J_0 \sin(\omega_{em} t)$  perpendicular to the surface  $S_2$ , and a Dirichlet boundary condition  $\Phi(\mathbf{X}, t) = 0$  is applied on the surface  $S_1$ . The input electrical current amplitude is  $J_0 = 200$  A for all problems. The initial conditions are  $\Phi(\mathbf{X}, 0) = \mathbf{0}$  and  $\mathbf{A}(\mathbf{X}, 0) = \dot{\mathbf{A}}(\mathbf{X}, 0) = \mathbf{0} \forall \mathbf{X} \in \Omega_0$ . The conductor is chosen to be aluminum with its known mechanical properties for the Young's modulus, density and Poissons ratio as 69 GPa, 2700 Kg/m<sup>3</sup> and 0.32 respectively. Correspondingly, the Lamé constants in Eq. (2) are  $\lambda = 46.5$  GPa and  $\mu = 26.1$  GPa. The electromagnetic properties in Eq. (6) are utilized as:  $\varepsilon = 8.2344 \times 10^{-11}$  F/m,  $\mu = 1.2567 \times 10^{-6}$  H/m and  $\sigma = 3.5461 \times 10^7$  S/m.

Simulations are conducted to study the effect of mechanical and electro-magnetic loadings on the multi-physics response. Representative results are summarized in Fig. 6(a) and (b). In the first example, the mechanical load amplitude and angular frequency are respectively  $u_0 = 0.2$  m and  $\omega_{me} = 200\pi$  (rad/s) and electric current angular frequency is  $\omega_{em} = 1000\pi$  (rad/s). This corresponds to a frequency ratio  $\frac{\omega_{em}}{\omega_{me}} = \frac{T_{me}}{T_{em}} = 5$ , where  $T_{me}$  and  $T_{em}$  are the

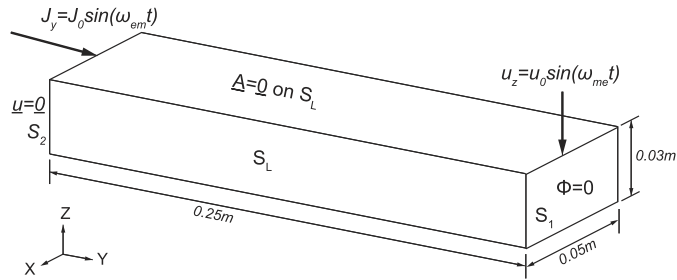


Fig. 5. Schematic model of a vibrating conductor with injected current. The mechanical loading is in  $z$ -direction and the electrical current is in  $y$ -direction.

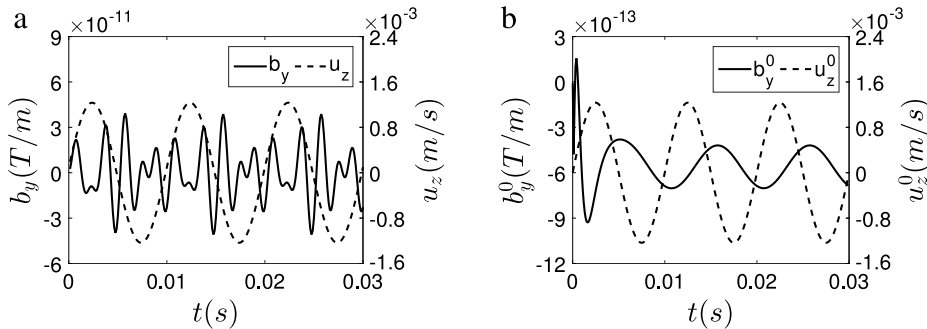


Fig. 6. Evolution of  $b_y$  and  $u_z$  with time for mechanical angular frequency  $\omega_{me} = 200\pi$  (rad/s) and electrical current angular frequencies (a)  $\omega_{em} = 1000\pi$  (rad/s) and (b)  $\omega_{em} = 20,000\pi$  (rad/s).

respective time periods. The evolution of the  $y$ -direction magnetic induction field in the current configuration and the  $z$ -direction displacement component at a point (0.025, 0.125, 0.015)m are plotted (for different scales) in Fig. 6(a). The frequency of electromagnetic response fields are affected by the frequencies of both the electrical current and mechanical loading. Two periods are seen in the response plots, viz. a shorter time period that follows the high frequency pattern of the imposed electrical current, and a longer time period (corresponding to the distance between two identical maximum peaks). The latter follows the frequency of the mechanical excitations.

In the second example, the frequency ratio is increased to  $\frac{\omega_{em}}{\omega_{me}} = 100$  with  $\omega_{em} = 20,000\pi$  (rad/s) and  $\omega_{me} = 200\pi$  (rad/s). The electromagnetic field solutions exhibit two distinct time scales in their response. The first corresponds to the frequency of the applied EM fields, while the second is related to the carrier frequency of the vibrating substrate. Since the first time-scale is very small in comparison with the latter, the EM solutions in Fig. 6(b) is representative only of the lower frequency response i.e. solutions corresponding to the beginning of each EM cycle. The plots in Fig. 6(b) include the results of  $y$ -direction magnetic induction field at the beginning of each EM cycle, along with the deformation field, plotted on different scales.

The figure illustrates that the lower frequency component of the EM response follows the frequency of the mechanical loading. The different electromagnetic and mechanical responses show that the EM fields evolve nonlinearly in different directions through the coupling with the nonlinear ME fields.

The effect of direct coupling between the EM and ME fields is investigated in Fig. 7, where the fully coupled solutions in Eqs. (41a) and (41b) are compared with configuration-based static solutions. The configuration-based static EM solutions correspond to those in the absence of the conductor velocity and acceleration fields, but in the respective deformed configurations. The electrical current angular frequency is  $\omega_{em} = 20,000\pi$  (rad/s). As seen with the  $y$ -direction electric field, the lack of explicit velocity field representation in the EM field solution in the configuration-based static solution, leads to considerable error in the EM field response. Hence it is important to solve the coupled problem in a rigorous manner. However, the coupling makes it difficult to solve electromagnetic fields for a large number of mechanical cycles, especially for problems with large frequency ratios ( $\frac{\omega_{em}}{\omega_{me}} \sim 10^5$ ), common in many practical problems. With increasing frequency ratios, coupled simulations using conventional, single time-

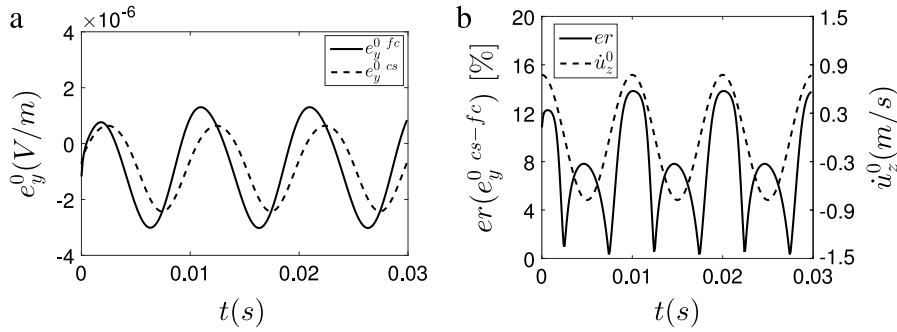


Fig. 7. Comparison of fully coupled (fc) and configuration-based static (cs) coupling of EM fields with ME variables for  $\omega_{em} = 20,000\pi$  (rad/s) (a)  $e_y$  and (b) evolution of error based on Eq. (19) in  $e_y$  with velocity field.

scale integration schemes become computationally prohibitive. Multi-time scale methods that can project the high frequency response on low frequency fields are needed to overcome this challenge.

Temporal scales in the coupled EM–ME problems are characterized by:

1. Fine time-scale  $\tau$  corresponding to the high frequency oscillations of the electromagnetic fields;
2. Coarse time-scale, characterized by the slow-scale variations of the maximum EM amplitude, which is a function of the mechanical cycles. This is represented and will be termed as the EM cycle-scale  $N$ .

The nonlinear finite deformation, semi-discrete equations (39) are solved using the Newton–Raphson iteration method, for temporally evolving nodal displacements  $u_i^\beta$  in the cycle-scale  $N$ . For the  $p$ -th iteration step at the  $N$ -th cycle, the equations solved are:

$$R_i^\alpha(N) \Big|_{p+1} = R_i^\alpha(N) \Big|_p + \frac{\partial R_i^\alpha(N)}{\partial u_j^\beta(N)} \Big|_p \Delta u_j^\beta(N) = 0 \implies$$

$$u_j^\beta(N) \Big|_{p+1} = u_j^\beta(N) \Big|_p + \Delta u_j^\beta(N) = u_j^\beta(N) \Big|_p - \left[ \frac{\partial R_i^\alpha(N)}{\partial u_j^\beta(N)} \Big|_p \right]^{-1} R_i^\alpha(N) \Big|_p \tag{43}$$

where the residual is obtained from Eqs. (39) as:

$$R_i^\alpha(t) = R_i^\alpha(N) = \sum_e \int_{V_{0,e}} Q^\alpha \rho_0 Q^\beta \ddot{u}_i^\beta dV$$

$$+ \sum_e \int_{V_{0,e}} \frac{\partial Q^\alpha}{\partial X_J} P_{iJ} dV - \sum_e \int_{V_{0,e}} Q^\alpha \rho_0 b_i dV - \sum_{S_{0,T}} \int_{S_0} Q^\alpha P_{iJ} N_J dS. \tag{44}$$

Equilibrium conditions are assumed in a weak sense for the mechanical problem during the evolution of electromagnetic fluxes. The parameters for an unconditionally stable Newmark-beta time integration are utilized as  $\gamma = 0.5$  and  $\beta = 0.25$  (see for details [29]). Thus, the time step  $\Delta N$  is chosen to satisfy accuracy constraints only [29,54]. For a tolerance set to  $10^{-3}$ , convergence in the iterative scheme is achieved for  $\frac{\Delta t}{T_{me}} = 0.02$ , i.e. 50 time steps per mechanical loading period. Thus, the maximum allowable EM cycles traversed in each increment of mechanical time integration is taken as:

$$\Delta N_{\max} = \frac{\omega_{em}}{50\omega_{me}}. \tag{45}$$

The FE representation of EM potentials  $\Phi^\beta(t)$  and  $A_I^\beta(t)$  in Eqs. (41a) and (41b) have a corresponding two-scale temporal representation, viz.

- (i)  $\{\Phi^\beta(N, \tau)\} = \{C_{IJ}(N), J(N), A_I^\beta(N, \tau), \dot{A}_I^\beta(N, \tau), t(N, \tau)\}$ , and
- (ii)  $\{\ddot{A}_I^\beta(N, \tau)\} = \{C_{IJ}(N), J(N), \Phi^\beta(N, \tau), \dot{\Phi}^\beta(N, \tau), A_I^\beta(N, \tau), \dot{A}_I^\beta(N, \tau), t(N, \tau)\}$ .

The wavelet transformation based multi-time scaling method invokes a transformation of the first and second time derivatives of these potentials  $\{\dot{Y}_I^\beta(N, \tau)\} = \{\dot{\Phi}^\beta(N, \tau), \dot{\Phi}^\beta(N, \tau), \dot{A}_I^\beta(N, \tau), \ddot{A}_I^\beta(N, \tau)\}$  in terms of the discrete

orthogonal, multi-resolution, wavelet basis functions for decoupling the fine-scale response from the cycle-scale response.

$$\dot{Y}_I^\beta(\mathbf{X}, t) \equiv \dot{Y}_I^\beta(\mathbf{X}, N, \tau) = \sum_{k=1}^n C_I^{\beta k}(\mathbf{X}, N) \psi_k(\tau) \quad \forall \tau \in \left[ \sum_i^N T_i, \sum_i^{N+1} T_i \right]. \quad (46)$$

The corresponding wavelet induced coefficients  $C_I^{\beta k}(\mathbf{X}, N)$  may be obtained by virtue of orthogonality as:

$$C_I^{\beta k}(\mathbf{X}, N) = \frac{1}{T} \int_{\sum_i^N T_i}^{\sum_i^{N+1} T_i} \dot{Y}_I^\beta(\mathbf{X}, N, \tau) \psi_k(\tau) d\tau \quad \text{where } k = 1, \dots, n. \quad (47)$$

Here  $C_I^{\beta k}(\mathbf{X}, N)$  are the EM cycle-scale wavelet coefficients of state variables  $\dot{Y}_I(\mathbf{X}, N, \tau)$ ,  $T$  is the time period of the externally applied electrical current and  $n$  is the number of basis functions. This sparse transformation relates the evolution of the state variables with the monotonic evolution of coefficients. This can be integrated using the incremental methods in the coarse time scale  $N$ . The selection of the multi-resolution based wavelet family is important to obtain a sparse representation in the transformed domain and is discussed next.

### 5.2. Determination of the optimal wavelet family

The efficiency of a sparse representation, as seen in Eq. (46), requires the selection of an optimal wavelet family, for which an arbitrary signal may be reconstructed with the least number of coefficients. This is investigated by comparing the solution of the transformed equations (47) with the reference solution of Eqs. (41a) and (41b) obtained by using a single time-scale integration scheme, over different electromagnetic cycles for different electrical current loadings. A total of 57 wavelet families [53] including (i) Daubechies, (ii) Symlets, (iii) Coiflets, (iv) Biorthogonals and (v) Reverse Biorthogonals, etc. are applied to Eq. (47). Two different electrical current excitations are imposed on the surface  $S_2$  in Fig. 5:

- (i) a harmonic signal  $J_I(t) = \sin(20000\pi t)$
- (ii) an arbitrary periodic signal  $J_I(t) = f(20000\pi t)$  as shown in Fig. 8.

Evolution of the cycle-scale electric field  $e_x$  and the velocity  $\dot{u}_z$  for the example in Section 5.1 with the harmonic input current are illustrated in Fig. 9(a). The corresponding fine time-scale error in  $e_x$  from Eq. (19) at the EM cycle  $N = 226$  (approximately third ME cycle) is plotted as a function of the number of wavelet coefficients in Fig. 9(b). The reconstruction with Daubechies-8 wavelet family has the least truncation error in representing the sinusoidal EM fields. The error is low for wavelet families with bases that have continuous second derivatives. In general, Daubechies- $I$  with higher  $I$  have better approximations of smoother functions due to improved multi-resolution features. The Bi-orthogonal- $I$  family gives the poorest approximations.

Fig. 10(a) and (b) show the cycle-scale electric field  $e_x$  and its error at the EM cycle  $N = 226$  for the arbitrary periodic electrical current input. Here however, the electromagnetic fields have different smoothness levels in different directions. For this case, the Daubechies-4 family is able to accurately capture the location of the turning points as indicated in Fig. 10(b), and hence yields a lower error. The magnitude of fluctuations produced by scaling and wavelet functions of Daubechies-8 family is in general smaller than that with Daubechies-4, while the number of fluctuations is larger. In this paper, the Daubechies-8 family is chosen to represent electromagnetic signals in the coupled FE model.

### 5.3. Solving fine time-scale equations

The discrete wavelet transformation of Eq. (47) using Daubechies-8 family is performed through the matrix operation

$$\tilde{C}_I^{\beta k}(\mathbf{X}, N) = \tilde{T}_{kl}(\tau) \dot{Y}_I^{\beta l}(\mathbf{X}, N, \tau) \quad \text{where } k = 1, \dots, n_{wav} \text{ and } l = 1, \dots, n. \quad (48)$$

Here  $\tilde{T}_{kl}$  represents the reduced discrete wavelet filter, discussed in Section 4.1, for the Daubechies-8 basis functions and  $\tilde{C}_I^{\beta k}(\mathbf{X}, N)$  are the non-zero wavelet coefficients of state variables  $\dot{Y}_I(\mathbf{X}, N, \tau)$ . By substituting Eq. (48) into

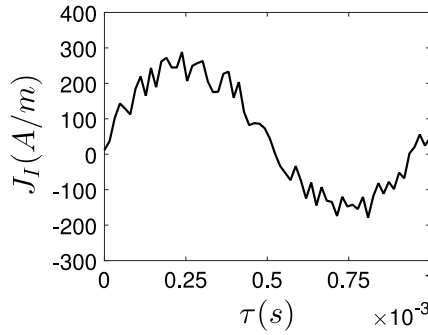


Fig. 8. Arbitrary periodic electrical current.

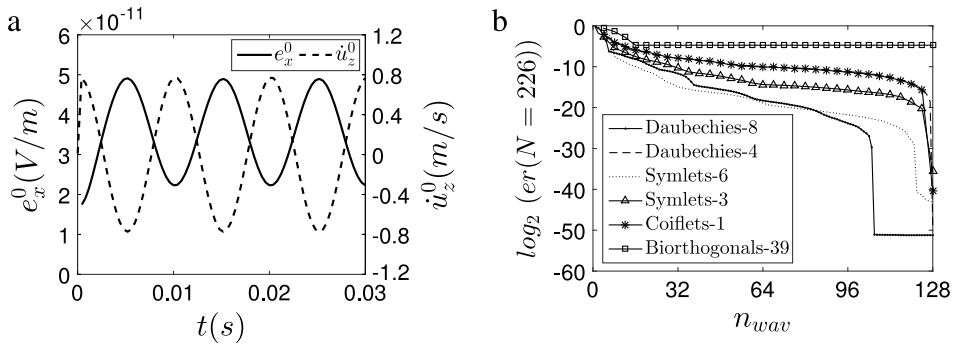


Fig. 9. (a) Reference solution for the x-component of electric field and (b) reconstruction error for a variety of wavelet families for a harmonic electrical current input.

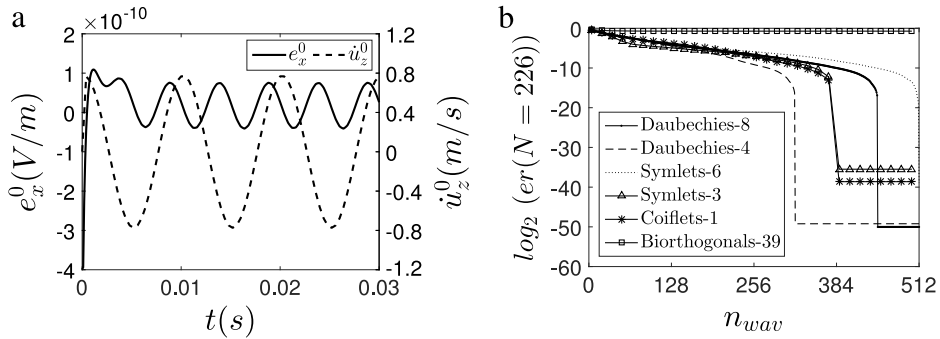


Fig. 10. (a) Reference solution for the x-component of electric field and (b) reconstruction error for a variety of wavelet families for an arbitrary periodic electrical current input.

Eqs. (41a) and (41b), the evolution of electromagnetic potentials is expressed as:

$$\dot{Y}_I^\beta(\mathbf{X}, N, \tau) = F^\beta(Y_I^\beta(\mathbf{X}, N, \tau), C_I^{\beta k}(\mathbf{X}, N), N, \tau). \tag{49}$$

With known coarse time scale initial conditions of the state variable  $Y_I^0(\mathbf{X}, N) = Y_I(\mathbf{X}, N, 0)$ , the cycle-scale electromagnetic responses are obtained by forward Euler integration as:

$$Y_I^\beta(\mathbf{X}, N, \tau) = \int_0^\tau \dot{Y}_I^\beta(\mathbf{X}, N, \tau') d\tau' = Y_I^\beta(\mathbf{X}, N, 0) + \int_0^\tau F^\beta(Y_I^\beta(\mathbf{X}, N, \tau'), C_I^{\beta k}(\mathbf{X}, N), N, \tau') d\tau'. \tag{50}$$

By substituting the inverse transform of Eq. (48) into Eq. (49), followed by substitution into Eq. (50), the semi-discrete FE equations (41a) and (41b) are now written in terms of discrete wavelet coefficients as:

$$\begin{aligned} \tilde{T}_{jl} \left( \int_0^{\tau_l} \tilde{T}_{lk}^T(\tau) d\tau \right) \tilde{C}_I^{\beta k}(\mathbf{X}, N) &= Y_I^\beta(\mathbf{X}, N, 0) \left( \sum_{l=1}^n \tilde{T}_{jl} \right) \\ &+ \sum_{l=1}^n \left( \tilde{T}_{jl} \int_0^{\tau_l} F^\beta \left( Y_I^\beta(\mathbf{X}, N, \tau), C_I^{\beta k}(\mathbf{X}, N), N, \tau \right) d\tau \right) \end{aligned} \quad (51)$$

where  $\tau_l = 0, \dots, T, j, k = 1, \dots, n_{wav}, l = 1, \dots, n$ . The forward Euler scheme is used to perform fine time scale integration in Eqs. (51) to obtain the cycle scale evolution of internal variables.

For efficient computing of the large degrees of freedom in the coupled ME–EM model, the finite element code is parallelized using available libraries. The ParMETIS library [55] is utilized to decompose the computational domain and distribute to multiple processors. Subsequently, the Portable, Extensible Toolkit for Scientific Computation or PETSc library [56], which is a Message Passing Interface (MPI) based library, is employed to accomplish code parallelization. Both the ME and EM codes are developed using PETSc to guarantee the same structure. The Newton–Krylov method [57], preconditioned with a complete Lower–Upper matrix factorization is used to solve the global system of equations (51).

#### 5.4. Solving coarse time-scale equations

The cycle-scale evolution of the initial conditions in Eq. (51) is determined by integrating one electromagnetic cycle in Eqs. (41a) and (41b) as:

$$\begin{aligned} \frac{dY_I^{\beta 0}}{dN}(\mathbf{X}, N) &= Y_I^\beta(\mathbf{X}, N, T) - Y_I^{\beta 0}(\mathbf{X}, N) \\ &= \int_0^T F^\beta \left( Y_I^\beta(\mathbf{X}, N, \tau), C_I^{\beta k}(\mathbf{X}, N), N, \tau \right) d\tau. \end{aligned} \quad (52)$$

Integrating the above equation by an implicit two-step, second order backward difference formula, yields a residual at the  $N$ -th cycle as

$$\begin{aligned} R_I^\beta(\mathbf{X}, N) &= \alpha_1 Y_I^{\beta 0}(\mathbf{X}, N) - \alpha_2 Y_I^{\beta 0}(\mathbf{X}, N - \Delta N) + \alpha_3 Y_I^{\beta 0}(\mathbf{X}, N - \Delta N - \Delta N_p) \\ &- \frac{dY_I^{\beta 0}}{dN}(\mathbf{X}, N) = 0 \end{aligned} \quad (53)$$

where

$$\begin{aligned} \alpha_1 &= \frac{(r+1)^2 - 1}{(r+1)^2 - (r+1)} & \alpha_2 &= \frac{(r+1)^2}{(r+1)^2 - (r+1)} & \alpha_3 &= \frac{1}{(r+1)^2 - (r+1)}, \quad \text{and} \\ r &= \frac{\Delta N_p}{\Delta N}. \end{aligned} \quad (54)$$

Here  $\Delta N$  and  $\Delta N_p$  are cycle jumps corresponding to the current and previous steps. The step sizes in Eqs. (53) and (43) should be chosen to guarantee stability of solution of the coupled system of equations. Eqs. (53) are solved using the Newton–Raphson iterative scheme. The Jacobian matrix for the above residuals can be obtained as

$$\frac{\partial R_I^i}{\partial Y_I^{j0}}(\mathbf{X}, N) = (\alpha_1 + \Delta N) I_{ij} - \Delta N \frac{\partial Y_I^{i0}(\mathbf{X}, N+1)}{\partial Y_I^{j0}(\mathbf{X}, N)} \quad (55)$$

where the partial derivative  $\frac{\partial Y_I^{i0}(\mathbf{X}, N+1)}{\partial Y_I^{j0}(\mathbf{X}, N)}$  corresponds to the change in the coarse time scale internal variables from cycle  $N$  to  $N + 1$ . This differentiation directly follows from applying the  $\tau$  scale response variation in Eq. (49)

recursively through the backward Euler scheme. For example  $ij$ -component of this matrix can be obtained as:

$$\frac{\partial Y_I^{i0}(\mathbf{X}, N+1)}{\partial Y_I^{j0}(\mathbf{X}, N)} = \prod_{k=1}^n \left[ 1 - \left[ \frac{\partial F^i}{\partial Y_I^j} \right] (\mathbf{X}, N, \tau_k) \Delta\tau \right]^{-1} \quad (56)$$

where  $n$  is the number of discretization points in the fine time scale response function. Note that for higher order representations of the cycle-scale derivative in Eq. (52), additional terms can be accommodated in Eq. (53). This will require simulating additional cycles for the response variation in Eqs. (56). Evaluating the tangent stiffness matrix in Eq. (55) requires global factorization at discrete time points within electromagnetic cycles followed by a multiplication over the time points. This calculation for the Newton–Raphson iteration is computationally exhaustive. Instead, a quasi-Newton method with a Broyden update for the stiffness matrix [29] is used to solve the evolution of coarse-scale variables. This iteration method has a super-linear convergence rate and is computationally much more efficient.

## 6. Adaptivity in the WATMUS method

The accuracy and efficiency of the WATMUS method depends on two parameters, viz. (i) the number of effective wavelet coefficients  $\tilde{C}_I^{\beta k}$  in Eq. (51) and (ii) the coarse time step  $\Delta N$  or the number of electromagnetic cycles traversed in each increment of the coarse time-scale integration. The former parameter depends on the chosen wavelet family and the form of the fine time-scale electromagnetic fields, while the latter is related to the truncation error in the coarse-scale time integration scheme. Criteria for adaptive augmentation of the WATMUS method have been developed for crystal plasticity finite element method in [40–42]. A similar method is implemented for the coupled problems in this paper.

### 6.1. Adaptive selection of evolving wavelet coefficients

Temporal wavelet transformation of the high-resolution state variables, increases the nodal degrees of freedom in the FE model by the number of coefficients  $n_{wav}$ , that are required to match the response. For high efficiency, it is prudent that an optimal number of wavelet basis functions  $n_{wav}$  be retained in the transformed representation. Coefficients that are essential in this representation and evolve with time are termed as “active”, while others are non-evolving, dormant coefficients. The set of evolving coefficients actively change during the temporal evolution of the FE model, thus controlling instability and inaccuracy in the solution. Only the active or evolving coefficients are solved in the set of global equations in (51).

In the adaptive criterion, the total set of wavelet coefficients for a state variable  $Y_I^\beta$  is expressed as a set  $\mathcal{I}_I = \{C_I^{\beta k} | k = 1 \dots n\}$ . This set is divided into evolving and non-evolving constituents, i.e.  $\mathcal{I}_I = \mathcal{I}_I^{evol} \cup \mathcal{I}_I^{non-evol}$ . The set of evolving coefficients in each increment of the cycle-scale problem is selected from the wavelet space, based on the criterion:

$$\mathcal{I}_I^{evol} = \left\{ C_I^{\beta k} | C_I^{\beta k+1} - 2C_I^{\beta k} + C_I^{\beta k-1} > \eta C_{I,tol}^{\beta k}, k = 1 \dots n_{wav} \right\} = \left\{ \tilde{C}_I^{\beta k}, k = 1 \dots n_{evol} \right\}. \quad (57)$$

Note that  $n_{evol}$  is analogous to  $n_{wav}$  in Eq. (51). The maximum value of all coefficients at each resolution is defined as:

$$C_{I,tol}^{\beta k} = \max_{2^{(log_2 k)} < l < 2^{(log_2 k)+1}} (C_I^{\beta l+1} - 2C_I^{\beta l} + C_I^{\beta l-1}) \quad (58)$$

and  $\eta$  is a tolerance. The complementary set of non-evolving coefficients, belonging to the entire set, is

$$\mathcal{I}_I^{non-evol} = \mathcal{I}_I - \mathcal{I}_I^{evol}. \quad (59)$$

The evolution of the state variable  $Y_I^\beta$  over an electromagnetic cycle is related to the complete set of wavelet coefficients through the relation

$$\begin{aligned}
 Y_I^\beta(\mathbf{X}, N, \tau_j) &= \sum_{k=1}^n T_{kj}(\tau) C_I^{\beta k}(\mathbf{X}, N) \quad j = 1, \dots, n \\
 &= \sum_{C_I^{\beta k} \in \mathcal{I}_I^{evol}} T_{kj}(\tau) C_I^{\beta k}(\mathbf{X}, N) + \sum_{C_I^{\beta k} \in \mathcal{I}_I - \mathcal{I}_I^{evol}} T_{kj}(\tau) C_I^{\beta k}(\mathbf{X}, N) \\
 &= \tilde{\mathbf{T}}^T(\tau) \tilde{C}_I(\mathbf{X}, N) + Y_I^{\beta add}(\mathbf{X}, N, \tau_j).
 \end{aligned} \tag{60}$$

The matrix  $\tilde{\mathbf{T}}$  is the reduced wavelet transform matrix constructed from the matrix  $\mathbf{T}$  by removing the rows associated with the non-evolving coefficients. The non-evolving coefficients remain constant during the cycle-scale representation and are denoted by  $Y_I^{\beta add}(\mathbf{X}, N, \tau_j)$ . The solution to Eq. (51) is enhanced by adding these coefficients.

6.1.1. Procedure for adding and removing wavelet coefficients

The procedure for adaptively adding and removing wavelet coefficients  $k = 1 \dots n_{wav}$  for improved accuracy and stability is discussed below.

1. Start with an initial guess on the set of evolving coefficients based on the criteria discussed in (57). As a starting procedure, simulating the first 20 electromagnetic cycles explicitly with single time-scale integration is found to yield satisfactory results.
2. Solve the problem in (51) for only the partial set of evolving coefficients. Then enhance the accuracy of the solution by adding  $Y_I^{\beta add}(\mathbf{X}, N, \tau_j)$ .
3. Solve the problem in (51), but now with the full set of wavelet coefficients  $\mathcal{I}_I$  for a given resolution. Compare with the solution in step 2 and evaluate the least square error below in the fine time-scale solution  $Y_I(N, \tau)$ , due to inclusion of the partial set.

$$er_I^\beta(N) = \frac{\left[ \sum_{i=1}^n \left( Y_{I(full)}^\beta(N, \tau_i) - Y_{I(partial)}^\beta(N, \tau_i) \right)^2 \right]^{1/2}}{\left[ \sum_{i=1}^n \left( Y_{I(exact)}^\beta(N, \tau_i) \right)^2 \right]^{1/2}}.$$

Based on the solution, select the additional set of evolving coefficients  $\mathcal{I}_I$ :

$$C_I^{\beta add} = \left\{ C_I^{\beta k} \mid C_I^{\beta k} \in \mathcal{I}_I^{non-evol} \quad \text{to satisfy } |er_I^\beta(N)| \leq \eta_e \right\}. \tag{61}$$

4. Go to Step 1.

This procedure ensures that an appropriate set of wavelet coefficients is selected such that fine time scale error in the state variables  $Y_I(\mathbf{X}, N, \tau)$  is bounded, following the lemma discussed below.

**Lemma 1.** Let  $Q_{j(full)}$  denote the full set of wavelet coefficients for a given resolution over the electromagnetic cycle  $N$  and  $Q_j$  represent the solution obtained by the procedure discussed in Section 6.1.1. Then

$$\left| Q_{j(full)} - Q_j \right| \leq n \max \left| K_{ji}^{-1}(\theta) \right| \max \left| P_i \right| \quad \forall i, j \in \mathcal{I} \text{ and } \theta \in (Q_j, Q_{j(full)}) \tag{62}$$

where  $P_i$  denotes the residual in Eq. (51) and  $K_{ij} = \frac{\partial P_i}{\partial Q_j}$ .

**Proof.** Using the Taylor series expansion of  $P_i$  about  $Q_j$ :

$$P_i(\mathbf{Q}_{(full)}) = P_i(\mathbf{Q}) + \sum_{j=1}^n \frac{\partial P_i}{\partial Q_j}(\theta) \left( Q_{j(full)} - Q_j \right) = 0 \quad \forall i, j \in \mathcal{I}. \tag{63}$$

Using uniqueness condition of the solution, Eq. (63) yields

$$Q_{i(full)} - Q_i = - \sum_{j=1}^n K_{ij}^{-1}(\theta) P_j. \tag{64}$$

The Cauchy Schwarz inequality leads to the condition

$$|Q_{i(full)} - Q_i| \leq \sqrt{\left\| \sum_{j=1}^n K_{ij}^{-1} \right\|^2 \left\| \sum_{j=1}^n P_j \right\|^2} \leq n \max |K_{ij}^{-1}(\Theta)| \max |P_j| \quad \forall i, j \in \mathcal{I}. \tag{65}$$

Numerically, it has been observed that components in the inverse positive definite matrix  $K_{ij}^{-1}(\Theta) \leq 1$ . Thus the error in the residual will be bounded when solving with a reduced set  $\mathcal{I}_I^{evol}$ . This is true as long as the error in the residual corresponding to the full set  $\mathcal{I}_I$  remains bounded.

6.2. Adaptive cycle increment selection in the time integration scheme

For the implicit second order backward difference method, used in the cycle-scale integration of the wavelet transformed equations, an adaptive cycle-scale incremental step control criterion is developed following the steps in [40,41]. This determines the optimal number of cycles  $\Delta N$  that can be traversed in each increment of the numerical time integration scheme. The optimal step size is controlled by the truncation error in the residual equation (53). For the backward difference scheme with a fixed increment  $\Delta N$ , the truncation error is derived from the truncation of second order terms in the Taylor’s expansion of the coarse time-scale state variable  $Y_I^{\beta 0}(\mathbf{X}, N)$  as:

$$\delta Y_I^{\beta 0} = \frac{1}{6} \left| \frac{\partial^3 Y_I^{\beta 0}}{\partial N^3} \frac{(r+1)^2 - (r+1)^3}{(r+1)^2 - 1} \right| \Delta N^3 \tag{66}$$

where  $r = \frac{\Delta N_p}{\Delta N}$  is the ratio of the previous to the current step size as defined in Eq. (54). This truncation error leads to the error in the residual  $\delta R_I$  of the cycle scale equilibrium equations as:

$$\delta R_I^\beta = \delta R_{I\ err}^\beta \frac{\Delta N^3}{6} \left( \frac{(r+1)^2 - (r+1)^3}{(r+1)^2 - 1} \right) \quad \text{where} \tag{67a}$$

$$\delta R_{I\ err}^\beta = (\alpha_1 + \Delta N) \frac{d^3 Y_I^i}{dN^3} - \Delta N \prod_{k=1}^n \left[ 1 - \left[ \frac{\partial F^i}{\partial Y_I^j} \right] \Delta \tau \right]^{-1} \frac{d^3 Y_I^j}{dN^3} \tag{67b}$$

$\alpha_1$  is defined in Eq. (54). For the error to be bounded by a prescribed tolerance  $\eta$ , the maximum allowable cycle step  $\Delta N$  is determined to be:

$$\Delta N \leq \min \left( \frac{6\eta R_I}{f \delta R_{I\ err}} \right)^{\frac{1}{3}} \quad \text{where } f = \frac{(r+1)^2 - (r+1)^3}{(r+1)^2 - 1} \tag{68}$$

with the residual  $R_I$  defined in Eq. (53).

A flowchart of the solution scheme, coupling the adaptive WATMUS-based electromagnetic and dynamic mechanical problems in a parallel setting is shown in Fig. 11.

7. Verification of the WATMUS-based coupled electromagnetic nonlinear dynamic FE model

The vibrating rectangular conductor, studied in Section 5.1, is further examined for accuracy and efficiency of the WATMUS method. The material properties, boundary and initial conditions are given in Section 5.1. The Daubechies-8 basis functions [53] are used to transform the fine time-scale electromagnetic field variables, evolving with the input electrical current frequency to the cycle-scale response evolving with the frequency of mechanical excitation. The starting procedure for the WATMUS requires single time-scale simulations for the first few cycles to obtain initial conditions for the cycle-scale problem with the residual given in Eq. (53). In this example, electromagnetic cycles corresponding to two time-steps of the mechanical problem are solved explicitly. Once the initial cycle-scale

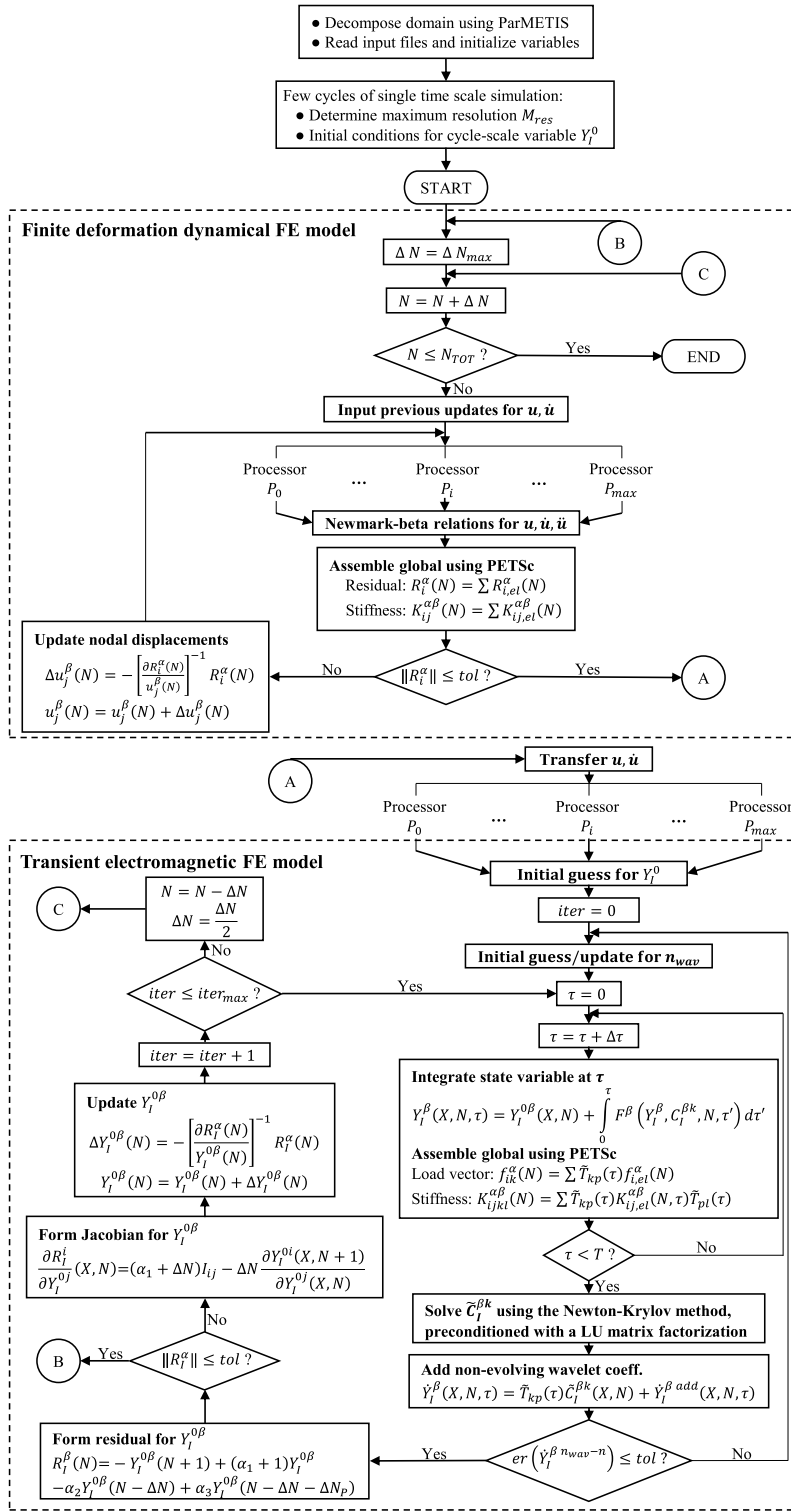


Fig. 11. Solution flowchart of the coupled ME-EM finite element model.

electromagnetic variables are derived, the program automatically switches to the cycle-scale mode where the time integration is performed in the  $N$  scale.

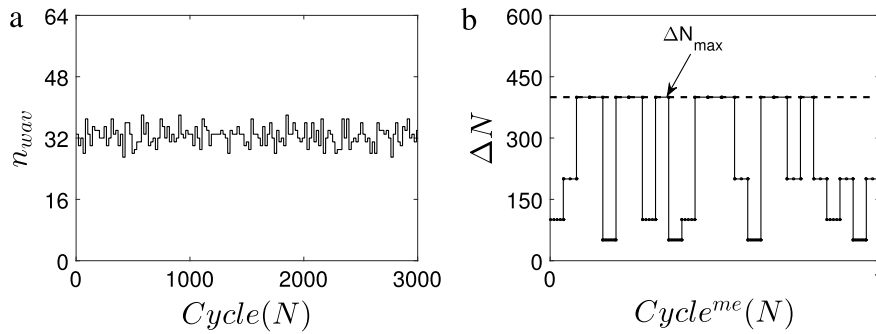


Fig. 12. Controlling parameters of adaptivity in the WATMUS method, for a mechanical excitation angular frequency  $\omega_{me} = 200\pi$  (rad/s): (a) varying number of evolving wavelet coefficients with EM cycles for an input electrical current angular frequency  $\omega_{em} = 20,000\pi$  (rad/s), (b) EM cycle increment selected with ME cycles, corresponding to an input electrical current angular frequency  $\omega_{em} = 2,000,000\pi$  (rad/s).

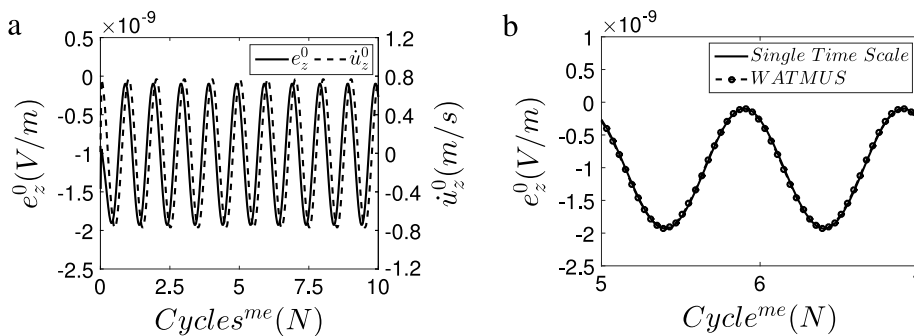


Fig. 13. (a) WATMUS solution of the cycle-scale electric field  $e_z$  and velocity  $u_z$  at a point ( $x = 0.025$  m,  $y = 0.125$  m,  $z = 0.015$  m), for  $\omega_{me} = 200\pi$  (rad/s) and  $\omega_{em} = 20,000\pi$  (rad/s), and (b) comparison of results by WATMUS and single time-scale integration schemes.

The controlling parameters of the adaptive process, viz. the number of evolving wavelet coefficients and coarse-scale, cycle increments as a function of cycles are illustrated in Fig. 12. In the example of Fig. 12(a) the frequency ratio is chosen to be  $\frac{\omega_{em}}{\omega_{me}} = 100$ . A tolerance of  $\eta_e = 10^{-2}$  is used to obtain an optimal number of coefficients. The number of wavelet coefficients  $n_{wav}$  actively changes with advancing EM cycles to improve the accuracy and stability of the EM field response. Fig. 12(b) shows the selected EM cycle increments within one ME cycle, for a different frequency ratio  $\frac{\omega_{em}}{\omega_{me}} = 10^4$ , using criteria established in Section 6.2. The maximum allowable step increment is chosen as  $\Delta N_{max} = 400$ , i.e. 400 EM cycles. A tolerance of  $\eta = 10^{-2}$  is used in Eq. (68) to predict the next increment step sizes.

Single time scale simulations are computationally expensive. Hence the lower frequency ratio  $\frac{\omega_{em}}{\omega_{me}} = 100$  is selected for comparing results up to 10 mechanical cycles of the coupled model with the WATMUS based results. The reference EM solution for comparison is taken to be the initial value of each EM cycle in the single time-scale simulations. Results of the  $z$ -direction electric field at a point ( $x = 0.025$  m,  $y = 0.125$  m,  $z = 0.015$  m) are compared with the WATMUS solution in Fig. 13. Fig. 13(a) shows the WATMUS-based EM solutions and the mechanical response for the 10 ME cycles, while Fig. 13(b) compares the WATMUS and single time-scale solutions over a portion of the ME cycles. Excellent agreement is seen in the two methods. The maximum time step in the WATMUS scheme is  $\Delta N = 4$ . The fine time-scale response for any EM cycle may be reconstructed from the wavelet basis functions and coarse time scale solutions.

For quantitative measures of the accuracy, two error measures are considered. The first compares the absolute value of the difference between the *cycle-scale state variables*  $Y_l^0(N)$  obtained by WATMUS and the single time-

scale integration (reference) methods, and is defined as:

$$er_I^{\beta 0}(N) = \frac{|Y_I^{\beta 0}(N) - Y_{I(ref)}^{\beta 0}(N)|}{|Y_{I(ref)}^{\beta 0}(N)|} \tag{69}$$

The second is a least-squares error of the difference in the *fine time scale state variables*  $Y_I(N, \tau)$  by the WATMUS and single time-scale integration (reference) schemes, as:

$$er_I^\beta(N) = \frac{\left[ \sum_{i=1}^n \left( Y_I^\beta(N, \tau_i) - Y_{I(ref)}^\beta(N, \tau_i) \right)^2 \right]^{1/2}}{\left[ \sum_{i=1}^n \left( Y_{I(ref)}^\beta(N, \tau_i) \right)^2 \right]^{1/2}} \tag{70}$$

Fig. 14(a) shows the fine time-scale solution  $e_z$ , reconstructed from the cycle-scale WATMUS solutions with 10, 20 and 64 wavelet coefficients respectively at  $N = 550$ . The fine time-scale percentage error for all the three components of the electric field with  $n_{wav} = 64$  and  $\Delta N = 4$  is illustrated in Fig. 14(b). The error in all three components of the fine time scale electric field solutions are within acceptable range with the controlling parameters. The WATMUS-based reconstructed electric field solution  $e_z$  with 10 and 20 wavelet coefficients give significant errors, while with 64 coefficients, the reconstructed field matches the fine-time scale results quite satisfactorily. The corresponding WATMUS-reconstructed solution for y-direction magnetic induction field is plotted in Fig. 15(a) and the error in all the three components is plotted in Fig. 15(b). Analogous to  $e_z$ , the reconstructed magnetic induction field solution  $b_y$  with 10 and 20 wavelet coefficients has significant errors. However with 64 wavelet coefficients, the  $b_y$  solution

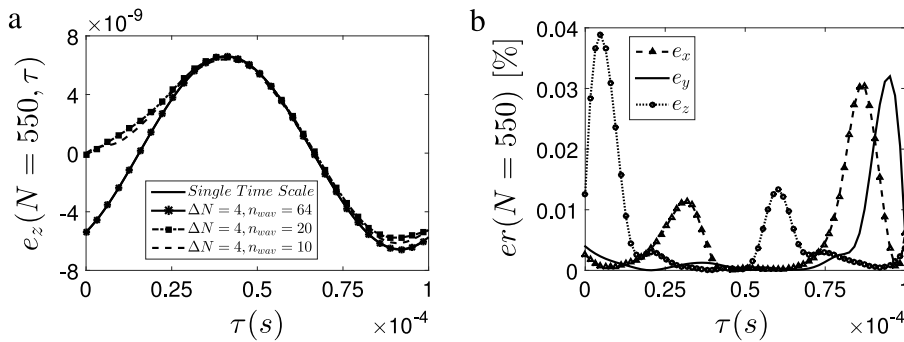


Fig. 14. (a) Fine time-scale electric field component  $e_z$  reconstructed from the cycle-scale WATMUS solutions for different wavelet coefficients at  $N = 550$ , and (b) error in all the three components of the electric field with  $\Delta N = 4$  and  $n_{wav} = 64$  within the 6th-ME cycle.

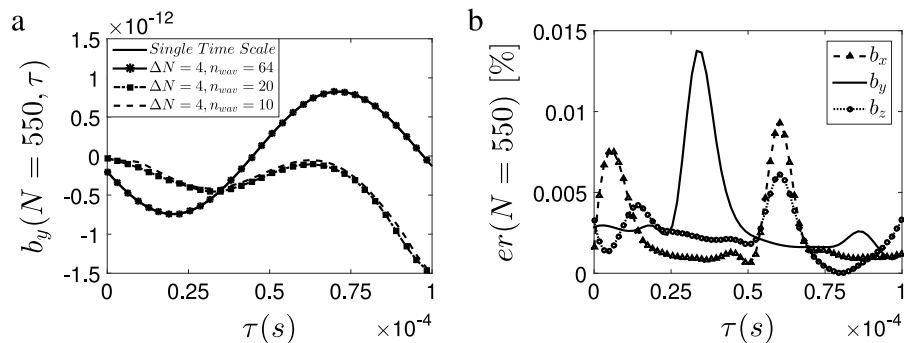


Fig. 15. (a) Fine time-scale magnetic induction field in y-direction reconstructed from the cycle-scale WATMUS solutions for different wavelet coefficients at  $N = 550$ , and (b) error in all the three components of the magnetic induction field with  $\Delta N = 4$  and  $n_{wav} = 64$  within the 6th-ME cycle.

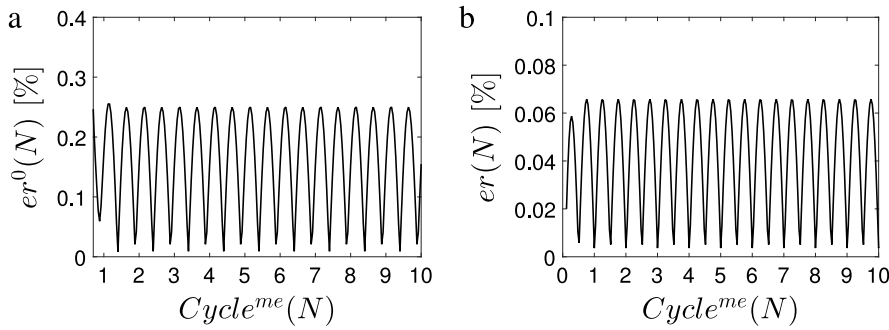


Fig. 16. Relative errors of the  $z$ -direction magnetic induction field in: (a) the coarse time-scale response, and (b) the fine time scale response.

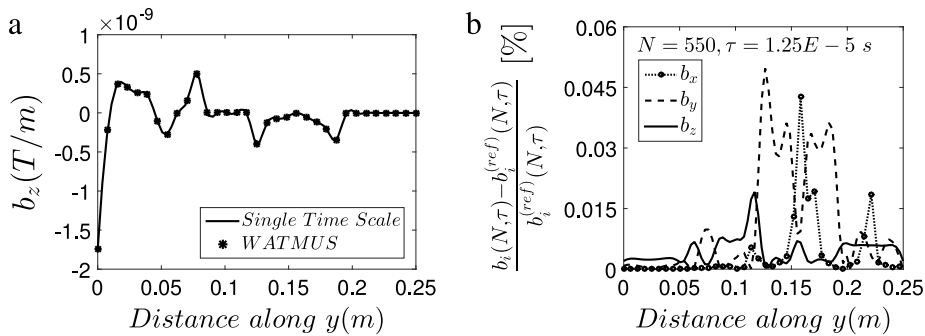


Fig. 17. The magnetic induction field in  $z$ -direction along a material line in the middle of the conductor at  $N = 550$  and  $\tau = 0.0000125$  s: (a) comparison of WATMUS and single time-scale solution, and (b) the relative error.

yields vastly reduced error in all the three components. The coarse and fine time-scale relative percentage errors in the  $z$ -direction magnetic induction field, given in Eqs. (69) and (70), are plotted as functions of the mechanical cycles in Fig. 16(a) and (b) respectively. The errors in the solutions are less than 0.251% and 0.0658% respectively. Finally, the evolution of the magnetic induction field  $b_z$  ( $N = 550$ ,  $\tau = 0.000125$  s) and the relative percentage error for all the three components of magnetic induction field along the center line in the  $y$ -direction ( $x = 0.025$  m,  $z = 0.015$  m) are shown in Fig. 17. The spatial distribution of the WATMUS-reconstructed magnetic induction field  $b_z$  is in agreement with the single time scale solution and the errors in all the three components along the center-line are within acceptable limits.

WATMUS simulations are next continued for 400 mechanical cycles. Contour plots of the  $z$ -direction magnetic induction field at  $(N, \tau) = (550, 1.25 \times 10^{-5}$  s) and  $(N, \tau) = (39550, 1.25 \times 10^{-5}$  s) with the magnetic field intensity vectors are shown in Fig. 18(a) and (b) respectively. The arrows in the figures correspond to the direction of the magnetic field solutions. Fig. 19 shows the evolution of  $b_z$  along a material line in the conductor with mechanical cycles from  $N_{me} = 6$  to  $N_{me} = 396$ . It is evident that different points in the conductor evolve differently with cycles. This makes extrapolation based results very inaccurate and establishes the need for the WATMUS method.

The results shown above are for a frequency ratio  $\frac{\omega_{em}}{\omega_{me}} = 100$ , for which the WATMUS method is about 6 times faster than the single time scale method.

### 7.1. Performance of the WATMUS-based FE model for large frequency ratios

The efficiency and accuracy of the WATMUS-based FE model are further examined in this section for higher frequency ratios of the electro-magnetic fields and dynamic oscillations. The rectangular conductor shown in Fig. 5 in Section 5.1 is simulated here, with the applied displacement on the surface  $S_1$  given as:

$$u_z(\mathbf{X}, t) = 0.2 \left( 1 + \alpha_{me} \left( 1 - \left( \exp\left(\frac{t}{t_m}\right) \right)^{\beta_{me}} \right) \right) \sin(\omega_{me} t).$$

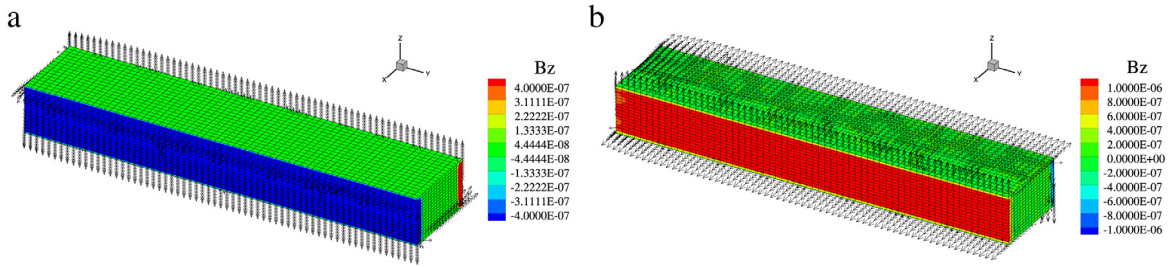


Fig. 18. Contour plots showing the WATMUS solution of  $z$ -direction magnetic induction field and magnetic field intensity vector at: (a)  $N = 550$  and  $\tau = 0.0000125$  s, (b)  $N = 39,550$  and  $\tau = 0.0000125$  s.

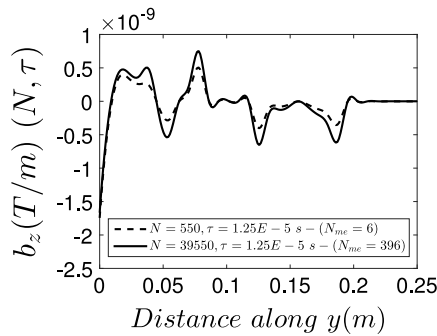


Fig. 19. Evolution of magnetic induction field in  $z$ -direction along a material line in the conductor with mechanical cycles from  $N_{me} = 6$  to  $N_{me} = 396$ .

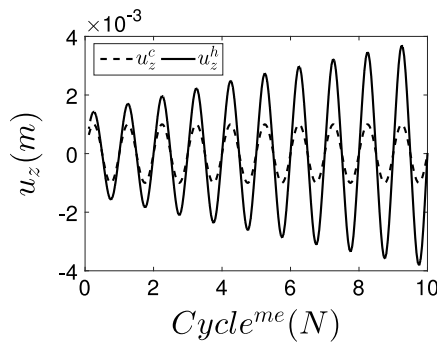


Fig. 20. Evolution of displacements  $u_z^h$  and  $u_z^c$ , at a location  $(0.025, 0.125, 0.015)$ m, for the variable amplitude and constant amplitude displacement excitations respectively in the rectangular conductor.

The displacement amplitude is changed to  $u_0 = 0.2 \left( 1 + \alpha_{me} \left( 1 - \left( \exp\left(\frac{t}{t_m}\right) \right)^{\beta_{me}} \right) \right)$ , to accentuate the temporal effects of the mechanical signal. The parameters affecting the initial conditions are considered to be  $\alpha_{me} = 10$ ,  $\beta_{me} = -1.5$  and  $t_m = 1$  s. The temporal evolution of the  $z$ -displacement component at a point  $(0.025, 0.125, 0.015)$ m for the evolving amplitude excitation, in comparison with a constant applied displacement amplitude  $u_0 = 0.2$ , is illustrated in Fig. 20. The mechanical angular frequency is  $\omega_{me} = 200\pi$  (rad/s). The variable amplitude excitation results in a transient electromagnetic response throughout the duration of the mechanical cycles. In the following subsections, the multi-physics response for electrical current excitations with two different frequency ratios, viz.  $\frac{\omega_{em}}{\omega_{me}} = 10^4$  and  $\frac{\omega_{em}}{\omega_{me}} = 10^6$  are studied.

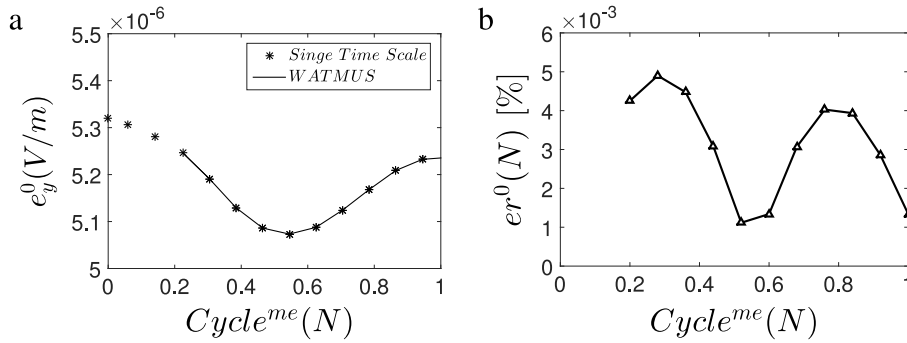


Fig. 21. (a) Comparison of the cycle-scale electric field  $e_y^0(N)$  obtained by the WATMUS method and single time-scale simulations for the 1st mechanical cycle, and (b) the corresponding percentage error in the response functions.

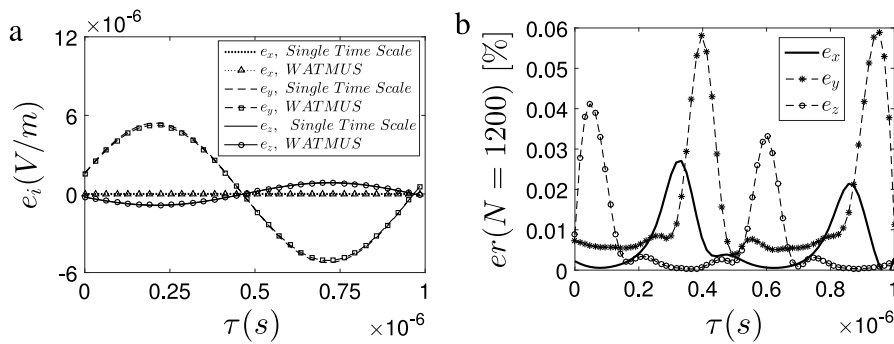


Fig. 22. (a) Comparison of the fine time scale electric field components  $e_i(N, \tau)$  reconstructed by the WATMUS method and the single time scale simulations, and (b) the corresponding error at  $N_{elec} = 1200$ .

7.1.1. Frequency ratio  $\frac{\omega_{em}}{\omega_{me}} = 10^4$

The electric current angular frequency is  $\omega_{em} = 2 \times 10^6\pi$  (rad/s) and the displacement angular frequency is  $\omega_{me} = 2 \times 10^2\pi$  (rad/s). Fig. 21(a) compares the coarse time scale  $e_y^0(N)$  obtained by the WATMUS method and the single time scale simulation at a point (0.025, 0.125, 0.015)m for only one mechanical cycle (it is computationally exhaustive to simulate more cycles with a single time-scale simulation). The corresponding coarse time-scale error is illustrated in Fig. 21(b). The fine time-scale electric field components  $e_i(N, \tau)$  in the current configuration are reconstructed from the cycle-scale WATMUS solutions with 64 wavelet coefficients. Fig. 22(a) compares the WATMUS reconstructed signal with the single time scale solution at  $N_{elec} = 1200$  that is within the 1st mechanical cycle. The corresponding relative percentage error in the components is plotted in Fig. 22(b). The plots indicate satisfactory accuracy of the WATMUS solutions. In terms of efficiency, the WATMUS method is found to be 50 times faster than the single time-scale method for this example.

Next, the coupled mechanical–electromagnetic problem is simulated for 50 mechanical cycles using the WATMUS method. The evolution of  $e_y^0(N)$  with mechanical cycles at the point (0.025, 0.125, 0.015)m is shown in Fig. 23(a). This corresponds to the evolution of the upper bound of electric field with mechanical cycles, i.e. the maximum value of electric field within each EM cycle. The displacement amplitude increases with the number of mechanical cycles and the upper bound of the cycle scale electric field  $e_y^0(N)$  has a moderate change with large cyclic mechanical vibrations. The figure in the inset shows a zoomed-in response for 5–10 mechanical cycles. The cycle scale magnetic induction field  $b_x^0(N)$ , shown in Fig. 23(b), starts with short harmonic oscillations and reaches nearly constant upper and lower bounds of  $2.469 \times 10^{-9}$  and  $-2.464 \times 10^{-9}$  respectively after 15 mechanical cycles. The fine time-scale electric and magnetic induction responses in the current configuration for  $N_{em} = 10^4$  and  $N_{em} = 5 \times 10^5$  are shown in Fig. 24. This corresponds to the responses in the first and 50th mechanical cycles. Comparing the peak electric field amplitudes for  $N_{em} = 10^4$  and  $N_{em} = 5 \times 10^5$ , the components  $e_x(N, \tau)$ ,  $e_y(N, \tau)$  and  $e_z(N, \tau)$  undergo a 645.13% increase, 18.63% decrease and 415.46% increase respectively. The magnetic induction field components, plotted in

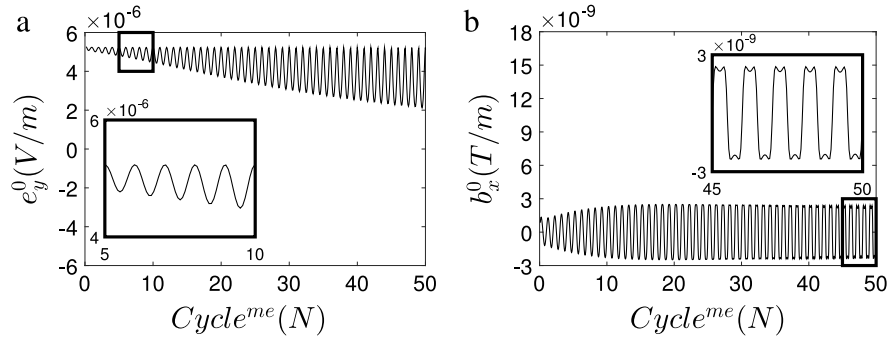


Fig. 23. Evolution of cycle scale (a) electric field  $e_y^0(N)$  and (b) magnetic induction field  $b_x^0(N)$  by the WATMUS method with cyclic deformation of the conductor. The figure in the inset shows the blowup response for 5–10 and 45–50 mechanical cycles respectively.

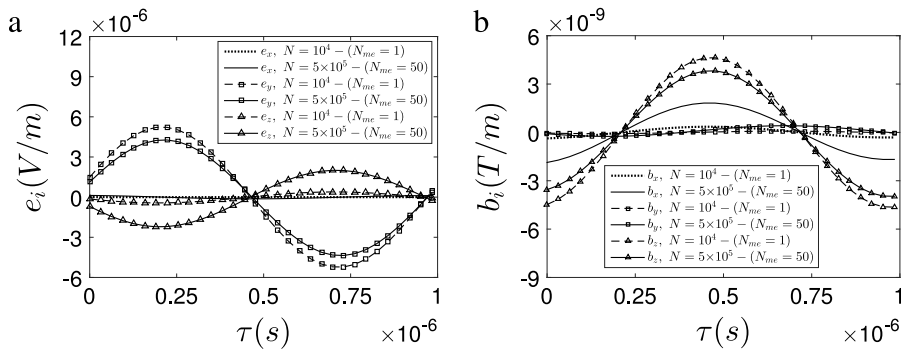


Fig. 24. Comparison of the (a) electric field  $e_i(N, \tau)$  and (b) magnetic induction field  $b_i(N, \tau)$  components for the 1st and 50th mechanical cycle obtained from WATMUS based simulations.

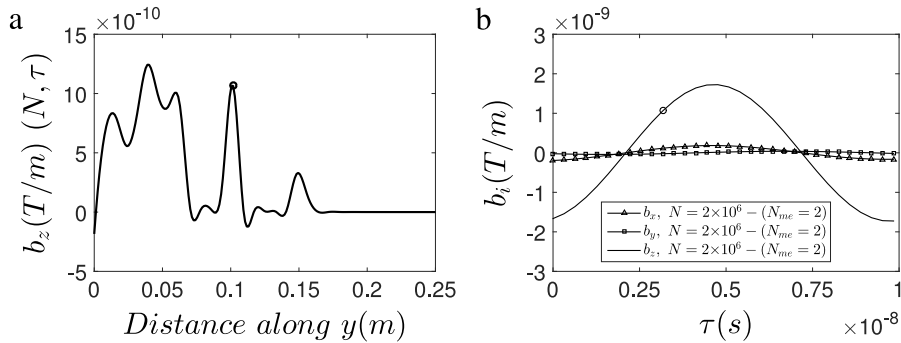


Fig. 25. (a) Evolution of magnetic induction field  $b_z$  along a material line at  $N = 2 \times 10^6$  and  $\tau = 3.125 \times 10^{-9}$  s, (b) magnetic induction field  $b_i(N, \tau)$  at  $N = 2 \times 10^6$  obtained from WATMUS based simulations for  $\frac{\omega_{em}}{\omega_{me}} = 10^6$ .

Fig. 24(b), correspondingly show a 45.16% increase, 221.90% decrease and 17.57% decrease for  $b_x(N, \tau)$ ,  $b_y(N, \tau)$  and  $b_z(N, \tau)$  respectively.

### 7.1.2. Frequency ratio $\frac{\omega_{em}}{\omega_{me}} = 10^6$

In this example, the electrical current angular frequency is increased to  $\omega_{em} = 2 \times 10^8 \pi$  (rad/s) and the ME–EM response is simulated for 2 mechanical cycles. The evolved magnetic induction field  $b_z(N = 2 \times 10^6, \tau = 3.125 \times 10^{-9}$  s) along a material line in the y-direction is shown in Fig. 25(a). The WATMUS-reconstructed fine time scale magnetic induction field components  $b_i(N, \tau)$  at  $N = 2 \times 10^6$  at a point ( $x = 0.025$  m,  $y = 0.1016$  m,  $z = 0.015$  m)

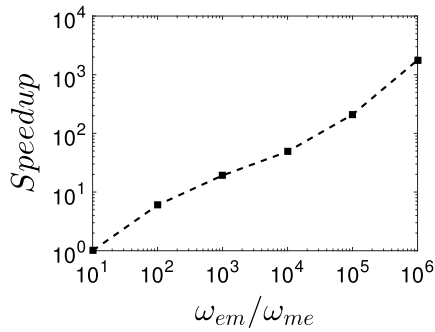


Fig. 26. Comparison of efficiency with various frequency ratios of  $\frac{\omega_{em}}{\omega_{me}}$  in WATMUS method.

are shown in Fig. 25(b). The WATMUS solution process is found to be 1500 times faster than the single time scale method for 200 EM cycles.

The computational time advantage in the simulations with various frequency ratios is shown in Fig. 26. The speedup advances non-uniformly at different stages of frequency ratios, depending on the effort required to satisfy the convergence criteria of the nonlinear multi-physics multi-time scaling problem.

## 8. Conclusions

An accurate and efficient, multi-time scale computational model is developed in this paper for coupled multi-physics analysis involving transient electromagnetic (EM) and dynamic mechanical (ME) fields. The computational method provides a flexible and robust platform for predicting time-dependent electromagnetic fields in a vibrating substrate for a range of high frequency electromagnetic fields and moderate frequency mechanical excitations. The coupled transient electromagnetic and dynamic governing equations are solved using a Lagrangian formation. Scalar and vector electromagnetic potentials are represented as variables in the finite element model. The coupled EM and ME boundary value problems are solved in a staggered manner. The entire computational model is parallelized using the ParMETIS library for decomposing the computational domain, and PETSc library for solving the system with a large number of degrees of freedom.

A novel, wavelet transformation induced multi-time scaling (WATMUS) method is introduced in the finite element framework to mitigate prohibitively high computational overhead incurred in time integration of the coupled multi-physics problems with large frequency ratios. The wavelet decomposition projects the high frequency response onto a low frequency cycle-scale problem through wavelet basis functions for numerical integration. No assumption of scale separation or periodicity is needed with this method. Stability is achieved through an implicit coarse-scale integration of the EM equations. An adaptive enhancement of WATMUS scheme allows for the selection of optimal wavelet bases in the transformation and integration step sizes. Error criteria are developed for optimally constructing the wavelet representation and for determining cycle steps to enhance computational efficiency and accuracy. The WATMUS method is applied to a reduced set of Maxwell's equations with arbitrary input EM signals, to satisfactorily assess the effectiveness of the multi-time scaling method.

Subsequently, the WATMUS method is implemented to solve deforming EM conductor problems with input harmonic electrical currents and harmonic mechanical excitations. Three frequency ratios, viz  $\frac{\omega_{em}}{\omega_{me}} = 100, 10^4$  and  $10^6$  are considered for the simulations. Characteristics of the coupled solutions clearly demonstrate the complexity brought about by coupling of two physical phenomena. Results from the WATMUS method show the accuracy and the highly improved computational efficiency in comparison with single time-scale methods. The cycle-scale solutions, along with reconstructed fine time-scale responses obtained from the WATMUS method agree very well with the single time scale solution, while providing significant computational efficiency advantage. In conclusion, the proposed WATMUS-based computational methodology is seen to have a tremendous potential in accurately simulating large number of electromagnetic cycles arising in real applications of multi-physics problems.

## Acknowledgments

This work was partially supported by the *Mechanics of Multifunctional Materials & Microsystems Program* of the Air Force Office of Scientific Research through a MURI grant on Bio-inspired Sensory Network to Stanford University. The specific work was done under a subcontract to Johns Hopkins University under award ID 2770925044895D. It has also been supported by the *Mechanics of Multifunctional Materials & Microsystems Program* of the Air Force Office of Scientific Research through a grant FA9550-14-1-0125. The program director for both of these grants is Dr. B.L. “(Les)” Lee. The authors gratefully acknowledge the support of this work. Computational support of this work has been provided by the Homewood High Performance Compute Cluster (HHPC) at Johns Hopkins University.

## Appendix. Boundary conditions for the transient Maxwell’s governing equations

Boundary conditions, in terms of scalar and vector potentials are obtained by replacing the field variables with potentials in the boundary terms of Eqs. (41a) and (41b), i.e.

$$\int_{\partial\Omega_0} N_I \left[ \varepsilon_0 J C_{IJ}^{-1} \left( -\Phi_{,J} - \dot{A}_J + \varepsilon_{JLK} \frac{\partial X_L}{\partial t} \varepsilon_{KMN} A_{N,M} \right) \delta\Phi \right] dS_0.$$

Dirichlet boundary conditions may be used for the applied voltage  $V = \Phi = \Phi_0$  in electrostatic problems or for grounded boundary  $\Phi = 0$ ,  $\delta\Phi = 0$ . Current injection condition, governed by Ohm’s law, can be expressed with the assumption of a fixed boundary as:

$$\int_{\partial\Omega_0} N_I \left[ \varepsilon J C_{IJ}^{-1} (-\Phi_{,J} - \dot{A}_J) \right] \delta\Phi dS_0 = \int_{\partial\Omega_0} N_I \left[ \varepsilon \frac{J_I}{\sigma} \right] \delta\Phi dS_0. \quad (\text{A.1})$$

For the weak form in Eq. (41b), the boundary terms corresponding to the Dirichlet type condition reduce to:

$$\int_{\partial\Omega_0} N_L \left[ \varepsilon_{KLM} \left( \frac{1}{\mu J} C_{MN} B_N + \varepsilon_{MRP} \frac{\partial X_R}{\partial t} \varepsilon J C_{PQ}^{-1} \tilde{E}_Q \right) \delta A_K \right] dS_0 - \frac{2}{p} \int_{\partial\Omega_0} A_{R,R} N_K \delta A_K dS_0. \quad (\text{A.2})$$

This boundary condition is associated with the Maxwell’s equation and the gauge condition. When values of  $A_I$  are prescribed on a boundary, both terms in Eq. (A.2) remain zero. This Dirichlet boundary condition is associated with zero magnetic field on the boundary. From Eq. (9b), it follows that when a magnetic flux is prescribed to the boundary, Eq. (A.2) will hold when the vector field  $N_I \times H_I$  is assigned to the boundary.

## References

- [1] J. Gaspar, T. Mann, T. Sreekantamurthy, V. Behun, Structural test and analysis of a hybrid inflatable antenna, in: 48th AIAA/ASME/ASCE/AHS/ASC Structures, Structural Dynamics, and Materials Conference, AIAA, 2007, pp. 1–17.
- [2] J. Neidhoefer, J. Ryan, B. Leahy, V. Tripp, Cooperative multi-disciplinary design of integral load bearing antennas in small UAVs, *Technology* 30332 (2009) 0844.
- [3] F. Le Chevalier, D. Lesselier, R. Staraj, Ground-based deformable antennas, in: *Non-standard Antennas*, John Wiley & Sons, Inc., Hoboken, NJ, USA, 2013.
- [4] J.-H. So, J. Thelen, A. Qusba, G.J. Hayes, G. Lazzi, M.D. Dickey, Reversibly deformable and mechanically tunable fluidic antennas, *Adv. Funct. Mater.* 19 (22) (2009) 3632–3637.
- [5] J. Thomas, M. Seth, G. Daehn, J. Bradely, N. Triantafyllidis, Forming limits for electromagnetically expanded aluminum alloy tubes: Theory and experiment, *Acta Mater.* 55 (8) (2007) 2863–2873.
- [6] M. Stiemeier, J. Unger, B. Svendsen, H. Blum, Algorithmic formulation and numerical implementation of coupled electromagnetic-inelastic continuum models for electromagnetic metal forming, *Internat. J. Numer. Methods Engrg.* 68 (13) (2006) 1301–1328.
- [7] T. Zohdi, On the computation of the coupled thermo-electromagnetic response of continua with particulate microstructure, *Internat. J. Numer. Methods Engrg.* 76 (8) (2008) 1250–1279.
- [8] T. Zohdi, Simulation of coupled microscale multiphysical-fields in particulate-doped dielectrics with staggered adaptive FDTD, *Comput. Methods Appl. Mech. Engrg.* 199 (49–52) (2010) 3250–3269.
- [9] L. Hirsinger, C. Lexcellent, Modelling detwinning of martensite platelets under magnetic and (or) stress actions on nimnga alloys, *J. Magn. Magn. Mater.* 254–255 (0) (2003) 275–277.
- [10] B. Kiefer, D. Lagoudas, Magnetic field-induced martensitic variant reorientation in magnetic shape memory alloys, in: *Recent Advances in Theoretical Mechanics*, *Philos. Mag.* 85 (33–35) (2005) 4289–4329 (special issue).

- [11] C. Landis, Non-linear constitutive modelling of ferroelectrics, *Curr. Opin. Solid State Mater. Sci.* 8 (1) (2004) 59–69.
- [12] W. Zhang, K. Bhattacharya, A computational model of ferroelectric domains. part I: model formulation and domain switching, *Acta Mater.* 53 (1) (2005) 185–198.
- [13] W. Zhang, K. Bhattacharya, A computational model of ferroelectric domains. part II: grain boundaries and defect pinning, *Acta Mater.* 53 (1) (2005) 199–209.
- [14] A. Semenov, A. Liskowsky, H. Balke, Return mapping algorithms and consistent tangent operators in ferroelectroelasticity, *Internat. J. Numer. Methods Engrg.* 81 (10) (2009) 1298–1340.
- [15] J. Li, Y. Chen, Analysis of a time-domain finite element method for 3-D Maxwell's equations in dispersive media, *Comput. Methods Appl. Mech. Engrg.* 195 (33–36) (2006) 4220–4229.
- [16] C. Miehe, D. Rosato, B. Kiefer, Variational principles in dissipative electro-magneto-mechanics: A framework for the macro-modeling of functional materials, *Internat. J. Numer. Methods Engrg.* 86 (10) (2011) 1225–1276.
- [17] D. Zäh, C. Miehe, Computational homogenization in dissipative electro-mechanics of functional materials, *Comput. Methods Appl. Mech. Engrg.* 267 (0) (2013) 487–510.
- [18] M. Kamlah, C. Liskowsky, R. McMeeking, H. Balke, Finite element simulation of a polycrystalline ferroelectric based on a multidomain single crystal switching model, *Int. J. Solids Struct.* 42 (9–10) (2005) 2949–2964.
- [19] M. Elhadrouz, B. Zineb, E. Patoor, Finite element analysis of a multilayer piezoelectric actuator taking into account the ferroelectric and ferroelastic behaviours, *Internat. J. Engrg. Sci.* 44 (15–16) (2006) 996–1006.
- [20] A. Semenov, H. Kessler, A. Liskowsky, H. Balke, On a vector potential formulation for 3d electromechanical finite element analysis, *Commun. Numer. Methods. Eng.* 22 (5) (2006) 357–375.
- [21] K. Ghandi, N. Hagood, Mathematics and control in smart structures, proceedings, in: SPIE: Bellingham, vol. 3039, 1997, pp. 97–112.
- [22] D. Pardo, L. Demkowicz, C. Torres-Verdín, M. Paszynski, A self-adaptive goal-oriented hp-finite element method with electromagnetic applications. part I: Electrostatics, *Internat. J. Numer. Methods Engrg.* 65 (8) (2005) 1269–1309.
- [23] D. Xue, L. Demkowicz, Modeling of electromagnetic absorption/scattering problems on curvilinear geometries using hp finite/infinite element method, *Comput. Methods Appl. Mech. Engrg.* 42 (7) (2006) 570–579.
- [24] D. Vu, P. Steinmann, A 2-D coupled BEM-FEM simulation of electro-elastostatics at large strain, *Comput. Methods Appl. Mech. Engrg.* 199 (17–20) (2010) 1124–1133.
- [25] S. Guo, S. Ghosh, A finite element model for coupled 3d transient electromagnetic and structural dynamics problems, *Comput. Mech.* 54 (2) (2014) 407–424.
- [26] A. Kovetz, *Electromagnetic Theory with 225 Solved Problems*, Oxford University Press, 2000.
- [27] J. Jin, *The Finite Element Method in Electromagnetics*, second ed., Wiley IEEE Press, 2002.
- [28] M. Sadiku, *Numerical Techniques in Electromagnetics*, second ed., CRC, 2000.
- [29] K. Bathe, *Finite Element Procedures*, Prentice Hall, 2006.
- [30] J.B. Keller, R.M. Lewis, *Asymptotic Methods for Partial Differential Equations: The Reduced Wave Equation and Maxwell's Equations*, Springer, US, 1995.
- [31] F. Molinet, I.V. Andronov, D. Bouche, *Asymptotic and Hybrid Methods in Electromagnetics*, IEE, London, 2005.
- [32] S. Manchiraju, M. Asai, S. Ghosh, A dual time scale finite element model for simulating cyclic deformation of polycrystalline alloys, *J. Strain Anal. Eng. Des.* 42 (4) (2007) 183–200.
- [33] Q. Yu, J. Fish, Temporal homogenization of viscoelastic and viscoplastic solids subjected to locally periodic loading, *Comput. Mech.* 29 (3) (2002) 199–211.
- [34] C. Oskay, J. Fish, Fatigue life prediction using 2-scale temporal asymptotic homogenization, *Internat. J. Numer. Methods Engrg.* 61 (3) (2004) 329–359.
- [35] H. Bhatt, A.Q. Khaliq, Higher order exponential time differencing scheme for system of coupled nonlinear Schrödinger equations, *Appl. Math. Comput.* 228 (0) (2014) 271–291.
- [36] Y. Liu, H. Yang, Shift operator method and Runge-Kutta exponential time differencing method for plasma, *Int. J. Light Electron Opt.* 122 (23) (2011) 2086–2089.
- [37] S. Cox, P. Matthews, Exponential time differencing for stiff systems, *J. Comput. Phys.* 176 (2) (2002) 430–455.
- [38] G. Beilkin, J. Keiser, L. Vozovoi, A new class of time discretization schemes for the solution of nonlinear PDEs, *J. Comput. Phys.* 147 (2) (1998) 362–387.
- [39] P. Whalen, M. Brio, J. Moloney, Exponential time-differencing with embedded Runge-Kutta adaptive step control, *J. Comput. Phys.* 280 (0) (2015) 579–601.
- [40] D.S. Joseph, P. Chakraborty, S. Ghosh, Wavelet transformation based multi-time scaling for crystal plasticity FE simulations under cyclic loading, *Comput. Methods Appl. Mech. Engrg.* 199 (33–36) (2010) 2177–2194.
- [41] S. Ghosh, P. Chakraborty, Microstructure and load sensitive fatigue crack nucleation in ti-6242 using accelerated crystal plasticity fem simulations, *Int. J. Fatigue* 48 (0) (2013) 231–246.
- [42] P. Chakraborty, S. Ghosh, Accelerating cyclic plasticity simulations using an adaptive wavelet transformation based multi-time scaling method, *Internat. J. Numer. Methods Engrg.* 93 (13) (2013) 1425–1454.
- [43] D. Nelson, *Electric, Optic, and Acoustic Interactions in Dielectrics*, Wiley, 1979.
- [44] A. Mota, J.A. Zimmerman, A variational, finite-deformation constitutive model for piezoelectric materials, *Internat. J. Numer. Methods Engrg.* 85 (6) (2011) 752–767.
- [45] L. Vu-Quoc, V. Srinivas, Y. Zhai, Finite element analysis of advanced multilayer capacitors, *Internat. J. Numer. Methods Engrg.* 58 (3) (2003) 397–461.
- [46] A. Acharya, A. Sawant, On a computational approach for the approximate dynamics of averaged variables in nonlinear ode systems: Toward the derivation of constitutive laws of the rate type, *J. Mech. Phys. Solids* 54 (2006) 2183–2213.

- [47] A. Taflove, S.C. Hagness, *Computational Electrodynamics: The Finite-difference Time-domain Method*, third ed., Artech, Norwood, MA, 2005.
- [48] V. Cizek, *Discrete Fourier Transforms and their Applications*, Taylor & Francis Inc., 1986.
- [49] J. Ramanathan, *Methods of Applied Fourier Analysis*, Birkhauser, 1998.
- [50] J. Walker, *A Primer on Wavelets and their Scientific Applications*, CRC Press, 1999.
- [51] G. Strang, T. Nguyen, *Wavelets and Filter Banks*, Wellesley College, 1996.
- [52] I. Daubechies, Ten lectures on wavelets, in: *CBMS-NSF Regional Conference Series in Applied Mathematics*, in: *Society for Industrial and Applied Mathematics*, vol. 61, SIAM, Philadelphia, PA, 1992, p. 194.
- [53] *Introduction to Wavelet Families*, Matlab, Mathworks, Wavelet Toolbox Edition, 2013.
- [54] K. Bathe, G. Noh, Insight into an implicit time integration scheme for structural dynamics, *Comput. Struct.* 98 (2012) 1–6.
- [55] G. Karypis, K. Schloegel, V. Kumar, *Parmetis Parallel Graph Partitioning and Sparse Matrix Ordering Library version 3.1*, Tech. Rep., Univ. Minnesota, Dept. Computer Science and Engineering, 2003.
- [56] S. Balay, J. Brown, K. Buschelman, V. Eijkhout, W.D. Gropp, D. Kaushik, M.G. Knepley, L.C. McInnes, B.F. Smith, H. Zhang, *PETSc users manual*, Tech. Rep. ANL-95/11 - Revision 3.4, Argonne National Laboratory, 2013.
- [57] D. Knoll, D. Keyes, Jacobian-free Newton-Krylov methods: a survey of approaches and applications, *J. Comput. Phys.* 193 (2) (2004) 357–397.